The effect of copper doping on the structural, optical, and electrical properties of cadmium oxide thin films using the spray pyrolysis technique

Fatemeh Davari
Damghan University
Mohammad Reza Fadavieslam (m.r.fadavieslam@du.ac.ir)
Damghan University https://orcid.org/0000-0003-3981-8697

Research Article

Keywords: Soda-lime Glass Substrates, Grain Size, Surface Roughness, Electrical Resistivity, Seebeck Coefficient, Carrier Concentration and Mobility, n-type Conductivity

Posted Date: February 23rd, 2021

DOI: https://doi.org/10.21203/rs.3.rs-216115/v1

The effect of copper doping on the structural, optical, and electrical properties of cadmium oxide thin films using the spray pyrolysis technique

F. Davari[1], M. R. Fadavieslam[1,*]

[1]School of Physics, Damghan University, Damghan, Iran.

Email address: m.r.fadavieslam@du.ac.ir

Tel: +98 2335220090

Fax: +98 2335220090

Abstract

In this study, the pure and Cu doped CdO thin films with various doping concentrations (0 to 5 at.%) were deposited on soda-lime glass substrates, using the chemical spray pyrolysis technique. The effects of Cu doping on the structural, optical, and electrical properties of thin films were, then, investigated. The films were characterized through X-ray diffraction (XRD), field emission scanning electron microscopy equipped with an energy dispersive x-ray analyzer (FESEM-EDX), atomic force microscopy (AFM), ultraviolet-visible spectroscopy, and electrical resistance; van der Pauw techniques were also used to measure the Hall effect. X-ray diffraction studies showed that the thin films were polycrystalline only with cadmium oxide phase with the cubic face-centered crystal structure and the preferred orientations were along (111), (200), (220), (311), and (311) planes. The FE-SEM and AFM images also showed that with an increase in Cu doping levels, the grain size and surface roughness of the thin films decreased from 472 to 38 nm and from 163 to 54 nm, respectively. The expected element compositions were confirmed by EDX. The optical bandgap of the thin films ranged from 2.42 to 2.56 eV, and as Cu dopant increased, so, too, the optical bandgap. As the Cu doping concentration increased from 0 to 5 (at.%), the electrical resistivity and Seebeck coefficient were found to increase from 3.74×10^{-4} to 8.77×10^{-3} Ω.cm and 8.28×10^{-6} to 2.52×10^{-5} v/k (at 100 C^o temperature difference), respectively; the carrier concentration and carrier mobility were also found to decrease from 3.24×10^{20} to 1.76×10^{20} cm^{-3} and from 55.5 to 4.05 cm^2/v.s, respectively. The Hall effect and thermoelectric studies revealed that the films exhibited an n-type conductivity.

1 Introduction

Electrical and optical properties are more significant in metal oxides such as cadmium oxide (CdO), tin oxide (SnO_2), indium oxide (In_2O_3), titanium oxide (TiO_2), zinc oxide (ZnO), and nickel oxide (NiO), this issue has never escaped the attention of optoelectronic industries (Benhaliliba, et al. 2012; Dounia, et al. 2016; Ramarajan, et al. 2020; Şahin 2019). CdO is an important II-VI semiconductor with an n-type high electrical conductivity of ~10^2-10^4 S/cm thanks to its native defects and good transparency, especially in the NIR spectral region, with a direct bandgap of 2.2–2.7 eV depending on the deviation from the ideal CdO stoichiometry (Zargar, et al. 2020). CdO has a cubic (NaCl) structure based on octahedral coordination around Cd atoms and an Fm-3m symmetry with $a = 4.695\ \dot{A}$ (Dakhel 2014a; Dakhel and Bououdina 2014; Sahare, et al. 2017). These suitable physical properties have helped CdO thin films to have applications in photovoltaic solar cells, optoelectronic devices, smart windows, panel displays, thermally insulating glass, gas sensor devices, transparent electrodes, photodiodes, liquid crystal displays, IR detectors, and anti-reflection coatings, to name but a few (Aydin, et al. 2019; Dakhel and Bououdina 2015; Elttayef, et al. 2013). However, the optoelectronic properties of CdO thin films need to be adjusted and tailored for many optoelectronic applications. It is possible to engineer the physical properties of cadmium oxide by doping it with different elements like Ni, Fe, Y, In, Sm, Al, F, Ga, W, B, Ni, Mn, Mo, In, Au, Ag, Mn, Eu, Cr, Ti, Sn, Yb, and Cu (Desai 2018; Hymavathi, et al. 2017a; Jadhav, et al. 2017; Raaif and Mohamed 2017; Sankarasubramanian, et al. 2018). It was experimentally observed that it is possible to control the optoelectronic properties of CdO by doping it with different types of metallic ions with ionic radii smaller and/or equal to that of host lattice atoms (Dakhel 2014a; Dakhel and Bououdina 2015; Noorunnisha, et al. 2020a). Conduction properties of CdO are caused by its intrinsic natural structural point defects. Cadmium interstitials (Mi) and oxygen vacancies (VO) are point defects responsible for n-type conduction and conduction properties. Therefore, doping metallic ions increases metal interstitials (Mi) and oxygen vacancies (VO) and can improve the conduction parameters (Çolak and Türkoğlu 2013; Dakhel 2014a). In general, Cu can be easily used as a dopant in Cd; In fact, because the ionic radius of Cu^{+2} with six coordinations (0.073 nm) is less than that of Cd^{+2} ion (0.095 nm), it could improve the conduction parameters (Dakhel and Bououdina 2014). The CdO-based thin films can be produced through all manner of techniques ranging from thermal evaporation (Alharbi and Qasrawi 2021), pulsed laser deposition (Mostafa and Menazea 2020), sputtering (Hymavathi, et al. 2017b), e-beam evaporation (Purohit, et al. 2017), sol-gel spin coating (Sahbeni, et al. 2020), chemical vapor deposition (CVD) (Sharma, et al. 2019), chemical bath deposition (Das and Mitra 2017), successive ionic layer adsorption and reaction (SILAR)

(Sharma, et al. 2020), and solution growth (Onwuemeka and Ekpunobi 2018), to spray pyrolysis (Noorunnisha, et al. 2020b). Among all these techniques, the spray pyrolysis technique presents some advantages over other techniques in terms of affordability and suitability, which also convinced us to opt for it. In this work, we have studied the effect of copper doped CdO thin films on their physical properties.

2. Experimental details

2.1. Film preparation

Thin films were deposited on soda-lime glass substrates using a typical spray pyrolysis coating system. A 0.1 M solution of cadmium acetate was prepared by dissolving 2.665 gr of cadmium acetate dehydrate ($Cd(CH_3COO)_2 \cdot 2H_2O$) in 100 cc deionized water. Copper chloride ($CuCl_2.2H_2O$) was dissolved in the precursor solution. The atomic ratio of copper per tin or $\frac{[cu]}{[Cd]}$ (at.%) was changed from 0 to 1, 2, 3, 4, and 5 (at.%) to examine the effects of the Cu content on the physical properties of the thin films. The solution was, subsequently, stirred well and heated for about 45 min at 50 ^{o}C until it became bright and suitable for spray. The substrate temperature in all samples was set to 340 °C with an accuracy of ± 5 °C using a digital temperature controller. The spray deposition rate was 10 mL/min, with a 35 cm distance between the nozzle and the substrate. The hot plate rotation speed was 30 rpm. Before preparing the films, glass substrates were cleaned with ethanol using an ultrasonic bath for 15 min and placed on a hot plate. Eventually, the system was allowed to cool naturally to room temperature for about 80 min. The thin films prepared from the spray solutions with an atomic ratio of copper per tin equal to 0, 1, 2, 3, 4, and 5 (at.%) were named S_1, S_2, S_3, S_4, S_5, and S_6, respectively.

2.2. Sample characterization

The structural properties were examined through X-ray diffraction (XRD), using a D8 Advance Bruker X-ray diffractometer with Cu–Kα radiation (λ = 0.154056 nm) spectra in a 2θ range of 10°–80°. The surface morphology was investigated by field emission scanning electron microscopy (FESEM; HITACHI S-4160) and atomic force microscopy (ARA-AFM Brisk). A Unico 1800 double-beam spectrophotometer was also utilized to record the optical absorption of the thin films at the 450-1000 nm wavelength.

3 Results and discussions

3.1 Structural characterization

Figure 1 shows the XRD patterns of the pure and Cu doped CdO thin films. In this figure, the diffraction patterns showed five diffraction peaks at 2θ equal: 32.72°, 37.89°, 55.01°, 65.71°, and 68.80°, corresponding to the (111), (200), (220), (311), and (311) planes, respectively. The peaks match the standard JCPDS data (05-0640) and confirm the structure of the pure CdO phase with a face-centered cubic crystal structure (Benhaliliba, et al. 2012; Chandiramouli and Jeyaprakash 2013; Sahare, et al. 2017). It can also be inferred from Figure 1 that the XRD peak intensity of the (111) plane is relatively higher than that of the other reflections, indicating that the CdO films have a preferential growth along the (111) direction (Dakhel 2014b; Elttayef, et al. 2013; Jadhav, et al. 2017; Sahare, et al. 2017; Sankarasubramanian, et al. 2014). Another interesting point is that Bragg's positions of the diffraction planes shift slightly due to Cu doping (Benhaliliba, et al. 2012; Sahare, et al. 2017). Otherwise, the results of XRD do not show any CdO, CuO, and metallic Cu structure in the films, suggesting that the incorporation of Cu ions in the CdO lattice does not affect its crystal structure (Menazea, et al. 2020). Typically, Cu doping in CdO thin films involves replacing the host Cd^{2+} ions with Cu^{2+} ions in the host CdO lattice. To ensure a successful replacement of the Cd^{2+} ions with Cd^{2+} ions, both elements must possess the same valance and a more or less equal ionic radius. However, the ionic radius of Cu^{2+} (0.73 $\dot{A}$) is smaller than that of Cd^{2+} (0.95 $\dot{A}$). When Cu^{2+} is introduced in the lattice site of CdO, it might be easy to diffuse in the host CdO material and easily replaces $Cd^{2+,}$ causing small voids in the host lattice. This explains the slight shifts in reflections from the Cu doped CdO vis-à-vis the corresponding reflections from the pure CdO films (Benhaliliba, et al. 2012; Jadhav, et al. 2017; Sahare, et al. 2017). However, the absence of any secondary phase in the XRD patterns indicates that Cu^{2+} ions are well assimilated in the CdO lattice.

The crystallite size (D_s) of the grains can be evaluated using the Scherrer's formula (Sahare, et al. 2017):

$$D_s = \frac{k\lambda}{\beta \cos\theta} \qquad (1)$$

where K is a constant (0.9), λ the wavelength of the X-ray, β broadening of the diffraction line measured at half of its maximum intensity (in radian), and θ Bragg's diffraction angle. Table 1 presents the variation of the measured grain size of the pure and Cu-doped CdO thin films.

The average crystallite size of the samples was determined by the Halder-Wagner method. In this method, the full width at half maximum of the physical profile can be written as follows:

$$\beta_{hkl}^2 = \beta_l \beta_{hkl} + \beta_G^2 \qquad (2)$$

where, β_l and β_G are the full width at half maximum of the Lorentzian and Gaussian functions. that the advantage of this method is that it gives more weight to the peaks at low- and mid-angle ranges, where the overlapping of the diffracting peaks is significantly less. Now, according to the Halder-Wagner method, the relation between the crystallite size and lattice strain, is given as follows (Rebhi, et al. 2009):

$$\left(\frac{\beta_{hkl}^*}{d_{hkl}^*}\right)^2 = \frac{1}{D_{H-W}} \frac{\beta_{hkl}^*}{{d_{hkl}^*}^2} + \left(\frac{\varepsilon}{2}\right)^2 \qquad (3)$$

where $\beta_{hkl}^* = \frac{\beta_{hkl} \cos\theta_{hkl}}{\lambda}$ and $d_{hkl}^* = \frac{2 \sin\theta}{\lambda}$. The plot of equation (2), with $\left(\frac{\beta_{hkl}^*}{{d_{hkl}^*}^2}\right)$ terms along X-axis and $\left(\frac{\beta_{hkl}^*}{d_{hkl}^*}\right)^2$ along Y-axis for each peak of the XRD pattern, is shown in Figure 2. The slope of the plotted straight line provides the average crystallite size, whereas the intercept gives the intrinsic strain of samples S_1, S_2, S_3, S_4, S_5, and S_6. The values of ε and $D_{W\text{-}H}$ are presented in detail in Table 1. As can be seen, there is an overall downward trend for the average crystallite size with an increment in Cu doping (Gupta, et al. 2011; Sahare, et al. 2017).

The dislocation density (*δ)*, which gives direct information about the defects in the crystal structure, can be calculated using the following relation (Sahare, et al. 2017):

$$\delta = \frac{1}{D_{H-W}^2} \qquad (4)$$

The dislocation density is defined as the "length of dislocation lines per unit volume of the crystal", and higher values of δ indicate lower crystallinity levels for the films. The variation of the calculated δ value of the pure and Cu doped CdO thin films is shown in Figure 3. It can be seen that as the doping concentration in the CdO films increases, so, too, does the δ value (Sahare, et al. 2017).

Figure 4 represents field emission scanning electron microscopy (FE-SEM) images to provide information about the effect of copper doped on the surface morphology of the thin films. As can be seen, grains are almost uniformly distributed over the surface and they were uniformly and spherically shaped in nature without any cracks and porosity in any of the samples (Jadhav, et al. 2017). The average grain size was estimated using FE-SEM images, the results of which can be seen in Table 2. These results indicate that when the doped Cu increases, it causes a reduction in the grain size; therefore, the morphology of the samples changes considerably with Cu doped (Çolak and Türkoğlu 2013; Sahare, et al. 2017). In general, this agrees well with the XRD results. An enhanced surface uniformity and better substrate coverage were observed in the Cu-doped CdO films, which is very important for the devices (Sahare, et al. 2017).

The thickness of the thin films was estimated via the cross-sectional FE-SEM micrographs (Figure 4), as presented in Table 2. The thin film thickness decreases from 780 to 612 nm when [Cu]/[Cd] increases from 0 to 5%.

The EDX technique was applied to study the elemental composition of the thin films. Figure 5 illustrates the typical EDX spectrum of the CdS thin film prepared with 0.1% (at.%) of Cu. The observed elemental peaks have confirmed the presence of Cd and Cu in a thin film.

The two- (2D) and three-dimensional (3D) surface morphology of the pure and Cu-doped CdO thin films obtained from the AFM analysis can be seen in Figure 6. The roughness and root mean square (RMS) values of the films on dimensions of a 5×5 μm^2 area are given in Table 2. The surface roughness of the CdO films decreases as the doping concentration of Cu increases (Gupta, et al. 2011; Sahare, et al. 2017; Sankarasubramanian, et al. 2018). The variation in surface roughness values indicates that the Cu doping affects the surface topography of the thin films.

3.2 Optical study

The optical properties of the prepared films were studied through transmittance and absorbance spectra. The optical absorption and transmittance spectra of the pure and Cu doped CdO thin films were recorded in the wavelength range of 450-1100 nm, which are shown in Figure 7 and Figure 8, respectively. Figure 7 shows the variation of absorption with wavelength. In general, the absorption of the thin films tends to decrease with the erasing value copper doped. Moreover, Figure 8 shows that the optical transmittance of the CdO thin films improves with Cu doping, with all of them showing a sharp transmittance drop at the fundamental absorption band edge (λ ~500 nm); This figure also shows that, in general, it is blue-shifted for Cu doped (Benhaliliba, et al. 2012; Sahare, et al. 2017). This sharp edge corresponds to electron excitation from the valence band to the conduction band and is related to the nature and value of the optical bandgap. Hence, the CdO: Cu thin films could be used as a buffer material in solar cells (Sahare, et al. 2017).

The direct optical band gap is obtained through optical absorption measurements, plotting $(\alpha h\vartheta)^2$ versus photon energy $h\vartheta$,and that Tauc's equation as follows:

$$(\alpha h\vartheta)^2 = \beta\left(h\vartheta - E_g\right) \qquad (5)$$

where α is the absorption coefficient, β is a constant, and E_g is the direct optical band gap for the pure and Cu-doped CdO films, as shown in Figure 9. For all the samples, each curve of $(\alpha h\vartheta)^2$ versus $h\vartheta$ exhibits an excellent straight-line fit over a higher energy range above the absorption edge, suggesting a direct optical transition near the absorption

edge. The obtained optical band gap values are listed in Table 3. The calculated bandgap energy of the pure and Cu-doped CdO films was found in the range of 2.42-2.51eV; The bandgap of the CdO: Cu films is close to each other and higher than the bulk value (2.30 eV) (Raaif and Mohamed 2017). Based on quantum confinement effects in nanoparticles, as the grain size changes, so, too, does the bandgap (Şahin 2019). The bandgap values are in good agreement with the reported literature (Benhaliliba, et al. 2012; Dakhel 2014b; Gupta, et al. 2011). Doping of metal ions into nanostructured semiconductor materials is known to introduce magnetic sp-d exchange interactions between (s-type) electrons and (p-type) holes, causing extra optical properties (Şahin 2019). The optical gap is 2.48 eV for the pure CdO thin film. It show "red-shifts" by 2.42 eV after 1% Cu dopant (Elttayef, et al. 2013; Jadhav, et al. 2017). It is maybe due to an increase in the average crystallite size (Elttayef, et al. 2013). Besides, it might be attributed to the structural modification of the CdO films. The structural modification of the CdO: Cu thin films could be due to the Cd interstitial replacement or substitution with copper ions. This copper atom introduces some additional energy levels in the CdO bandgap close to the valance band edge. This might result in a reduction in transition energy (Jadhav, et al. 2017). The optical gap thin films with Cu dopant higher than 1% are greater than the pure CdO thin film (Benhaliliba, et al. 2012; Dakhel 2014b; Şahin 2019). These values show that the energy bandgap increases through doping which is usually attributed to the Moss-Burstein (B-M) effect (Benhaliliba, et al. 2012; Dakhel 2014a; Dakhel 2014b). Under the BM effect, optical band gap widening occurs as the Fermi level is raised into the conduction band of a degenerate nanostructured metal-oxide material (Şahin 2019). The effect of electron confinement in thin films can increase the bandgap energy by the decrease average crystallite size, and grain size (Vigil, et al. 2001). It can happen as a result of an increase in the amorphous nature, which in turn causes a decrease in the average crystallite size and grain size, according to XRD and FESEM results, respectively. That explains why, in this case, the rate of the electron-hole recombination becomes lower compared to the pure CdO thin film (Menazea, et al. 2020). Another possible reason for the broadening in the optical band gap energy via the doping process can be the impurity bands closer to the lower edge of the conduction band as a result of the Cd site in CdO, which are occupied by Cu atoms; these atoms have a strong orbital coupling with O atoms (Şahin 2019). Therefore, the valence electrons are excited to a higher energy level in the conduction band because they cannot occupy the states already occupied by the Pauli Exclusion Principle (Al-Ghamdi, et al. 2014; Manikandan, et al. 2017). It is possible, at high-level copper doping, for copper oxide in its amorphous structure to accumulate on grains and crystallite boundaries, increasing the values of transmittance and bandgap (Dakhel 2014b).

3.3 Electrical properties

The electrical properties of the pure and Cu doped CdO thin films were studied using the Hall measurement at room temperature in the van der Pauw configuration. The results are presented in Table 3. The variations of resistivity (ρ), carrier concentration (n), and mobility (μ) with the Cu dopant CdO thin films are also shown in Figure 10. The resistivity of either deposited pure films or Cu-doped films was found to range from 3.74×10^{-4} to 1.01×10^{-2} Ω.cm;

our measured values of resistivity are in good agreement with another study (Sankarasubramanian, et al. 2018). In general, it can be noticed that the electrical resistivity of the films drastically increases as the Cu concentration in the CdO films increases (Dakhel 2014b; Sankarasubramanian, et al. 2018). The grain boundary scattering mechanism can contribute to the controlling of the mobility of the current carriers in the films; otherwise, the mobility is mainly controlled by impurity and lattice scattering mechanisms. According to the FE-SEM images, an increase in the Cu dopant can cause a reduction in the grain size. Therefore, the boundary grains increase, which in turn further scatters the free carriers away from the grain boundaries. Finally, resistance increases (Şahin 2019). It should be noted that the increasing resistivity by the Cu dopant CdO film can be attributed to the influence of scattering mechanisms like phonon and ionized impurity scattering (Sankarasubramanian, et al. 2018). In general, carrier concentration and mobility decreased, while electrical resistivity increased as a result of Cu doping. However, the variation of carrier concentration with Cu doping is small compared to the variation in other electrical parameters. This can be explained by considering that Cu dopant ions have an identical valency as that of Cd ions. Thus, Cu doping affects n by occupying Cd-ion vacancies and/or interstitial positions (Dakhel 2014b). The negative sign of the Hall coefficient strongly confirms the n-type conducting nature of the thin films. This suggests that the Cu atoms are placed into the CdO lattice sites and act as a donor by supplying free electrons when they occupy the sites of Cd^{2+} (Sankarasubramanian, et al. 2018).

The thermoelectric e.m.f. of the CdO: Cu films was measured by applying a temperature gradient between the two ends of the samples. Figure 11 shows the variation of the thermoelectric emf versus the temperature difference in the thin films. The variation trend of the thermoelectric emf versus the temperature difference in the thin films was linear, which could be attributed to the increase in the carrier concentration and mobility of the charge carriers with rising temperatures (Sayas and Fadavieslam 2020). The negative slope in the thermo-EMF plots (Figure 11) shows that the thin films are n-type semiconductors in nature. These results tie in nicely with the results of the Hall effect measurement. The thermo-EMF of all the presented data shows an increase in magnitude with respect to the temperature difference. This may be attributed to the rise in the mobility charge carrier with a rise in temperature (Anwar, et al. 2015a; Anwar, et al. 2015b). The thermoelectric emf depends on the location of the Fermi energy in the material, the type of the scattering mechanism, and the density of the charge carriers. It increases as the Fermi energy moves further into the energy gap from the bottom edge of the conduction band. It, therefore, inevitably follows that the smaller the carrier concentration, the larger the Seebeck coefficient (Fadavieslam, et al. 2016). For a better

perspective, Sebeck coefficient $\left(\alpha = \frac{\varepsilon}{\Delta T}\right)$ at the 100 C^{o} temperature difference of all the samples is presented in Table 2. Decreased carrier density causes an increase in the Seebeck coefficient (Cappelli, et al. 2015).

4. Conclusion

In this paper, thin films of CdO: Cu with different contents of Cu% were prepared on soda-lime glass substrates, using the spray pyrolysis technique. Their structural, optical, and electrical properties were, then, studied. The XRD results show that the thin films exhibit a polycrystalline nature, and the incorporation of Cu ions in the CdO lattice does not change their crystal structure. The FE-SEM and AFM study shows that the spherically shaped grains and surface roughness decreased with an increase in the copper doping level. The optical properties of the thin films are sensitive to Cu doped. All the deposited films had a good transmittance and optical band gap for optoelectronic device applications, both of which increase with a Cu concentration in the CdO films. The electrical characteristics of the thin films show that all of them are n-type and their electrical resistivity increases as the doped Cu increases.

References

Al-Ghamdi, Ahmed A., et al: Semiconducting properties of Al doped ZnO thin films. Spectrochimica Acta Part A: Molecular and Biomolecular Spectroscopy **131** 512-517 (2014)

Alharbi, Seham Reef, A. F. Qasrawi: Effects of Au nanoslabs on the performance of CdO thin films designed for optoelectronic applications. Physica E: Low-dimensional Systems and Nanostructures **125** 114386 (2021)

Anwar, Sharmistha, et al: Spray pyrolysis deposited tin selenide thin films for thermoelectric applications. Materials Chemistry and Physics **153** 236-242 (2015a)

Anwar, Sharmistha, et al: Effect of deposition time on lead selenide thermoelectric thin films prepared by chemical bath deposition technique. Materials Science in Semiconductor Processing **34** 45-51 (2015b)

Aydin, R., H. Cavusoglu, B. Sahin: Transition metal Mn/Cu co-doped CdO transparent conductive films: Effect on structural, morphological and optical characteristics. Journal of Alloys and Compounds **785** 523-530 (2019)

Benhaliliba, M., et al: Luminescence and physical properties of copper doped CdO derived nanostructures. Journal of Luminescence **132**(10) 2653-2658 (2012)

Cappelli, E., et al: Nano-crystalline Ag–PbTe thermoelectric thin films by a multi-target PLD system. Applied Surface Science **336** 283-289 (2015)

Chandiramouli, R., B. G. Jeyaprakash: Review of CdO thin films. Solid State Sciences **16** 102-110 (2013)

Çolak, Hakan, Orhan Türkoğlu: Structural and electrical studies of Cu-doped CdO prepared by solid state reaction. Materials Science in Semiconductor Processing **16**(3) 712-717 (2013)

Dakhel, A. A: Improving carriers mobility in copper and iron-codoped CdO. Materials Science in Semiconductor Processing 17 194-198 (2014a)

A.A.Dakhel: Optical and electrical properties of copper-doped nano-crystallite CdO thin films. Solid State Sciences **31** 1-7 (2014b)

Dakhel, A. A., M. Bououdina: Development of transparent conducting copper and iron co-doped cadmium oxide films: Effect of annealing in hydrogen atmosphere. Materials Science in Semiconductor Processing **26** 527-532 (2014)

A. A. Dakhel, M. Bououdina: Structural, optical, and magnetic properties of Cu- and Ni-codoped CdO dilute magnetic nanocrystalline semiconductor: effect of hydrogen post-treatment. Applied Physics A 119(3) 1053-1060 (2015)

Das, Mahima Ranjan, Partha Mitra: Influence of Mn incorporation on ionic conductivity and dielectric relaxation process in CBD synthesized CdO thin films. Journal of Alloys and Compounds **724** 614-624 (2017)

Desai, S. P.: Improved opto-electrical properties of spray deposited ytterbium doped cadmium oxide thin films. Journal of Materials Science: Materials in Electronics **29**(17) 14416-14426 (2018)

Dounia, R., et al: Preparation and characterization of highly transparent and conductive indium-zinc oxide thin films deposited by pyrolysis spray technique. Optical and Quantum Electronics **48**(6) 339 (2016)

Elttayef, Abdul-Hussein K., Hayder M. Ajeel, and Ausama I. Khudiar: Effect of annealing temperature and doping with Cu on physical properties of cadmium oxide thin films. Journal of Materials Research and Technology **2**(2) 182-187 (2013)

Fadavieslam, M. R., H. Azimi-Juybari, M. Marashi: Dependence of O2, N2 flow rate and deposition time on the structural, electrical and optical properties of SnO2 thin films deposited by atmospheric pressure chemical vapor deposition (APCVD). Journal of Materials Science: Materials in Electronics **27**(1) 921-930 (2016)

Gupta, R. K., F. Yakuphanoglu, F. M. Amanullah: Band gap engineering of nanostructure Cu doped CdO films. Physica E: Low-dimensional Systems and Nanostructures **43**(9) 1666-1668 (2011)

Hymavathi, B., B. Rajesh Kumar, T. Subba Rao: Influence of sputtering power on structural, electrical and optical properties of reactive magnetron sputtered Cr doped CdO thin films. Journal of Materials Science: Materials in Electronics **28**(10) 7509-7516 (2017a)

Hymavathi, B., B. Rajesh Kumar, T. Subba Rao: Thickness dependent optical dispersion parameters and nonlinear optical properties of nanostructured Cr doped CdO thin films. Optical and Quantum Electronics **49**(2) 86 (2017b)

Jadhav, Gurunath, et al: Effect of Copper Doping on Physical Properties of Cadmium Oxide Thin Films, Recent Trends in Materials and Devices **178** 163-167 (2017)

Manikandan, A., et al: Rare earth element (REE) lanthanum doped zinc oxide (La: ZnO) nanomaterials: Synthesis structural optical and antibacterial studies. Journal of Alloys and Compounds 723 1155-1161 (2017)

Menazea, A. A., Ayman M. Mostafa, Emad A. Al-Ashkar: Impact of CuO doping on the properties of CdO thin films on the catalytic degradation by using pulsed-Laser deposition technique. Optical Materials **100** 109663 (2020)

Mostafa, Ayman M., A. A. Menazea: Laser-assisted for preparation ZnO/CdO thin film prepared by pulsed laser deposition for catalytic degradation. Radiation Physics and Chemistry **176** 109020 (2020)

Noorunnisha, T., et al: (Zn + Co) co-doped CdO thin films with improved figure of merit values and ferromagnetic orderings with low squareness ratio well suited for optoelectronic devices and soft magnetic materials applications. Applied Physics A **126**(10) 762 (2020a)

Noorunnisha, T., et al: Improved Haacke's quality factor and paramagnetic-to-ferromagnetic transition realized in Ni co-doped CdO:Zn thin films. Journal of Materials Science: Materials in Electronics **31**(15) 12169-12177 (2020b)

Onwuemeka, Joseph Ijeoma, Azubuike Josiah Ekpunobi: Synthesis of CdO:SnO2 alloyed thin films for solar energy conversion and optoelectronic applications. Journal of Materials Science: Materials in Electronics **29**(11) 9176-9183 (2018)

Purohit, Anuradha, et al: Substrate dependent physical properties of evaporated CdO thin films for optoelectronic applications. Physics Letters A **381**(22) 1910-1914 (2017)

Raaif, M., S. H. Mohamed: The effect of Cu on the properties of CdO/Cu/CdO multilayer films for transparent conductive electrode applications. Applied Physics A **123**(6) 441 (2017)

Ramarajan, R., et al: Enhanced optical transparency and electrical conductivity of Ba and Sb co-doped SnO2 thin films. Journal of Alloys and Compounds **823** 153709 (2020)

Rebhi, A., T. Makhlouf, and N. Njah: X-Ray diffraction analysis of 99.1% recycled aluminium subjected to equal channel angular extrusion. Physics Procedia **2**(3) 1263-1270 (2009)

Sahare, Sanjay, et al: A Comparative Investigation of Optical and Structural Properties of Cu-Doped CdO-Derived Nanostructures. Journal of Superconductivity and Novel Magnetism **30**(6) 1439-1446 (2017)

Sahbeni, K., et al: Effect of CdO ratios on the structural and optical properties of CdO–TiO2 nanocomposite thin films. Journal of Materials Science: Materials in Electronics **31**(4) 3387-3396 (2020)

Şahin, Bünyamin: Dual doping (Cu with rare-earth element Ce): An effective method to enhance the main physical properties of CdO films. Superlattices and Microstructures **136** 106296 (2019)

Sankarasubramanian, K., et al: Enhancing resistive-type hydrogen gas sensing properties of cadmium oxide thin films by copper doping. New Journal of Chemistry **42**(2) 1457-1466 (2018)

Sankarasubramanian, K., et al: Structural, optical and electrical properties of transparent conducting hydrophobic cadmium oxide thin films prepared by spray pyrolysis technique. Superlattices and Microstructures **69** 29-37 (2014)

Sayas, M. R., and M. R. Fadavieslam: Influence of deposition conditions on structural, electrical, and optical properties of cadmium oxide thin films deposited using the spray pyrolysis technique. Journal of Materials Science: Materials in Electronics **31**(21) 18320-18335 (2020)

Sharma, A. K., et al: Nanostructured CdO–ZnO composite thin films for sensing application. Journal of Materials Science: Materials in Electronics (2020)

Sharma, A.K., et al: Influence of bath temperature on microstructure and NH3 sensing properties of chemically synthesized CdO thin films. Materials Science-Poland **37**(1) 25-32 (2019)

Vigil, O., et al: Structural and optical properties of annealed CdO thin films prepared by spray pyrolysis. Materials Chemistry and Physics **68**(1) 249-252 (2001)

Zargar, Rayees Ahmad, et al: Screen printing coating of (ZnO)0.8(CdO)0.2 material for optoelectronic applications. Optical and Quantum Electronics **52**(9):401 (2020)

Figure Captions

Fig. 1. XRD patterns for samples S_1, S_2, S_3, S_4, S_5, and S_6

Fig. 2. Typical Halder-Wagner plots of samples S_1, S_2, S_3, S_4, S_5, and S_6

Fig. 3 Variations of the average crystallite size ($D_{H\text{-}W}$), dislocation density (δ), and strain (ε) as a function of the [Cu]/[Cd] % molar ratio in the thin films

Fig. 4. Top view FE-SEM and cross-section FE-SEM images of samples S_1, S_2, S_3, S_4, S_5, and S_6

Fig. 5 Energy-dispersive X-ray analysis spectra of a thin film with [Cu]/[Cd]=1%

Fig. 6. AFM images of samples S_1, S_2, S_3, S_4, S_5, and S_6 (a) two dimensional and (b) three dimensional

Fig. 7. Variation of absorption versus wavelength in samples S_1, S_2, S_3, S_4, S_5, and S_6

Fig. 8. Variation of transmittance versus wavelength in samples S_1, S_2, S_3, S_4, S_5, and S_6

Fig. 9. Plots of $(\alpha h\vartheta)^2$ versus $h\vartheta$ for samples S_1, S_2, S_3, S_4, S_5, and S_6

Fig. 10. Variations of resistivity (ρ), carrier concentration (n), and electron mobility (l) as a function of the [Cu]/[Cd] % molar ratio in the thin films

Fig. 11. Variation of the thermoelectric emf versus the temperature difference in samples S_1, S_2, S_3, S_4, S_5, and S_6

Table Captions

Table 1. Results of the XRD characterization of the thin films

Table 1. Results of the morphology characterization of the thin films

Table 3. Results of the electrical characterization of the thin films

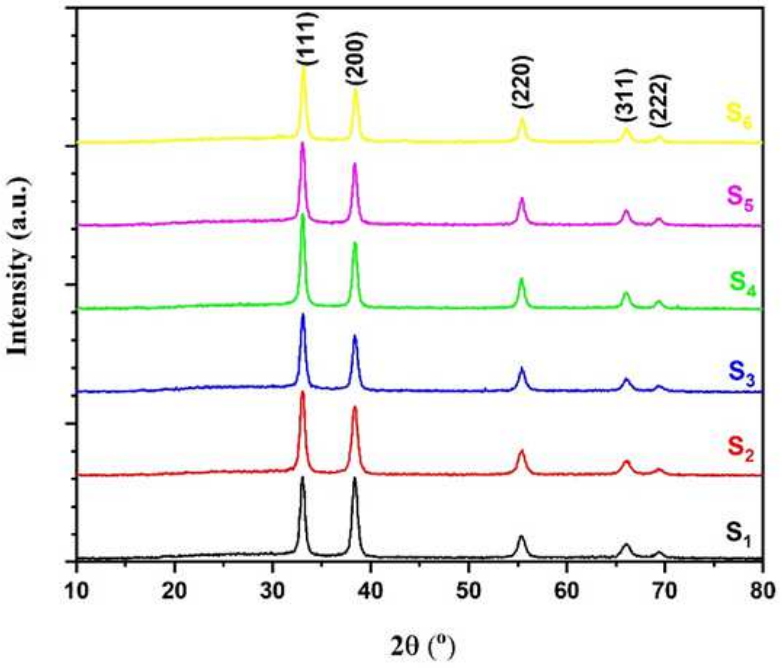
(111)
(200)
(220)
(311)
(222)
S6
S5
S4
S3
S2
S1
Intensity (a.u.)
10
20
30
40
50
60
70
80
2θ (°)

Figure 1

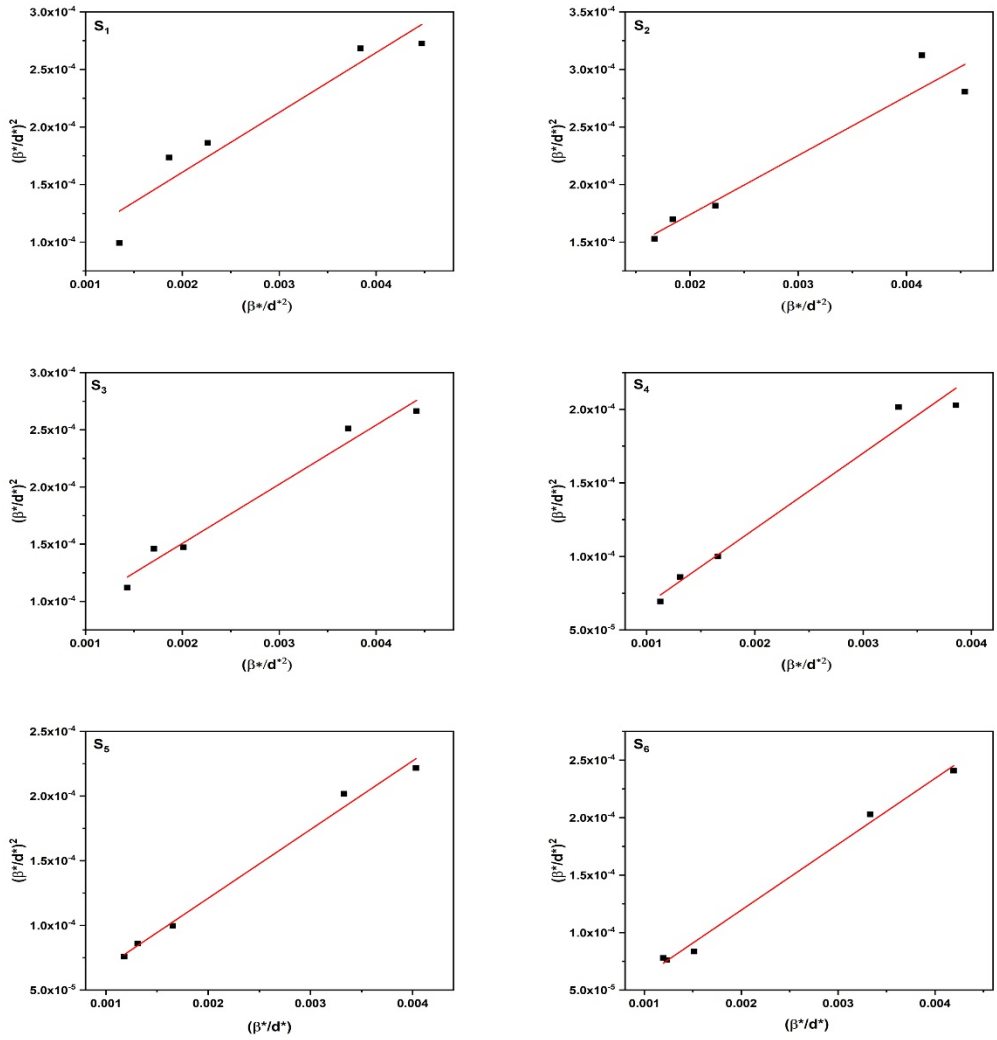

Figure 2

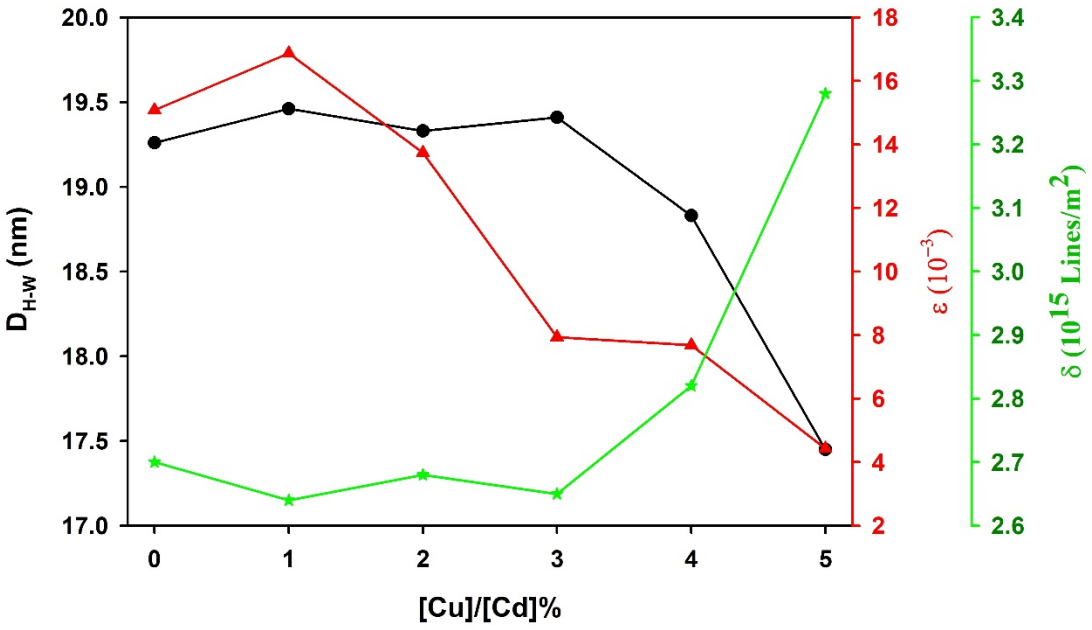
20.0
19.5
19.0
18.5
18.0
17.5
17.0
D_{H-W} (nm)
18
16
14
12
10
8
6
4
2
ε (10^{-3})
3.4
3.3
3.2
3.1
3.0
2.9
2.8
2.7
2.6
δ (10^{15} Lines/m^2)
0
1
2
3
4
5
[Cu]/[Cd]%

Figure 3

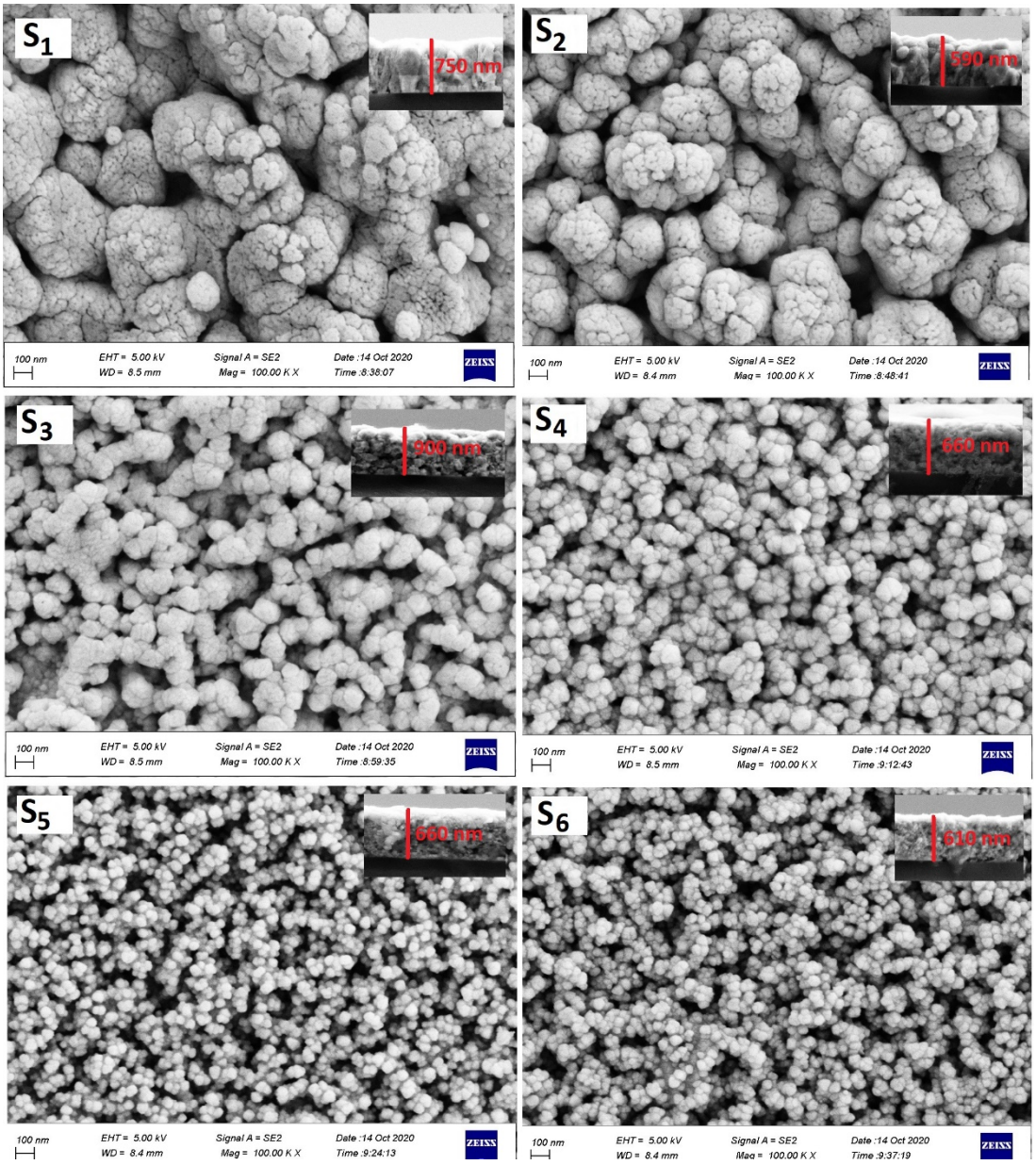
S1
750 nm
100 nm
EHT = 5.00 kV
WD = 8.5 mm
Signal A = SE2
Mag = 100.00 K X
Date :14 Oct 2020
Time :8:38:07
ZEISS
S2
590 nm
100 nm
EHT = 5.00 kV
WD = 8.4 mm
Signal A = SE2
Mag = 100.00 K X
Date :14 Oct 2020
Time :8:48:41
ZEISS
S3
900 nm
100 nm
EHT = 5.00 kV
WD = 8.5 mm
Signal A = SE2
Mag = 100.00 K X
Date :14 Oct 2020
Time :8:59:35
ZEISS
S4
660 nm
100 nm
EHT = 5.00 kV
WD = 8.5 mm
Signal A = SE2
Mag = 100.00 K X
Date :14 Oct 2020
Time :9:12:43
ZEISS
S5
660 nm
100 nm
EHT = 5.00 kV
WD = 8.4 mm
Signal A = SE2
Mag = 100.00 K X
Date :14 Oct 2020
Time :9:24:13
ZEISS
S6
610 nm
100 nm
EHT = 5.00 kV
WD = 8.4 mm
Signal A = SE2
Mag = 100.00 K X
Date :14 Oct 2020
Time :9:37:19
ZEISS

Figure 4

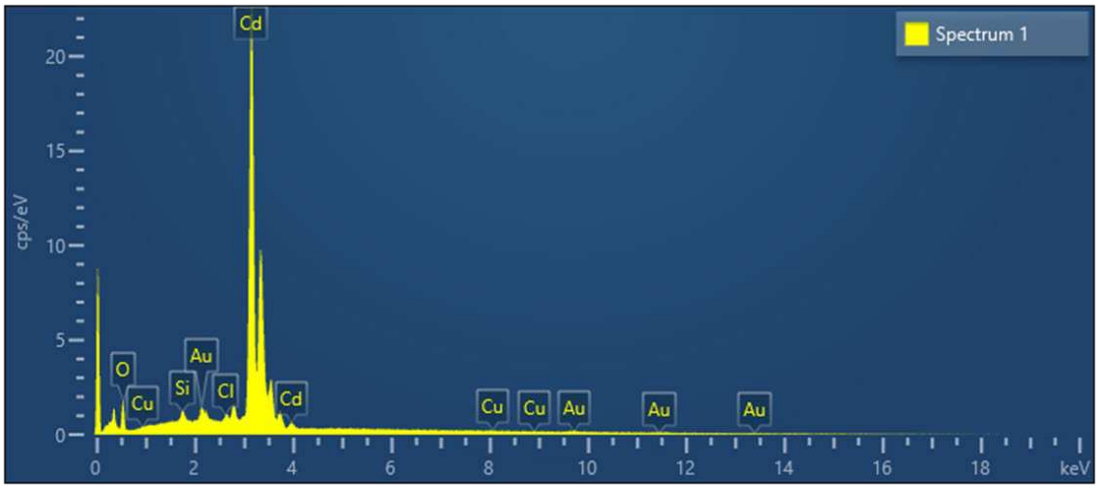

Figure 5

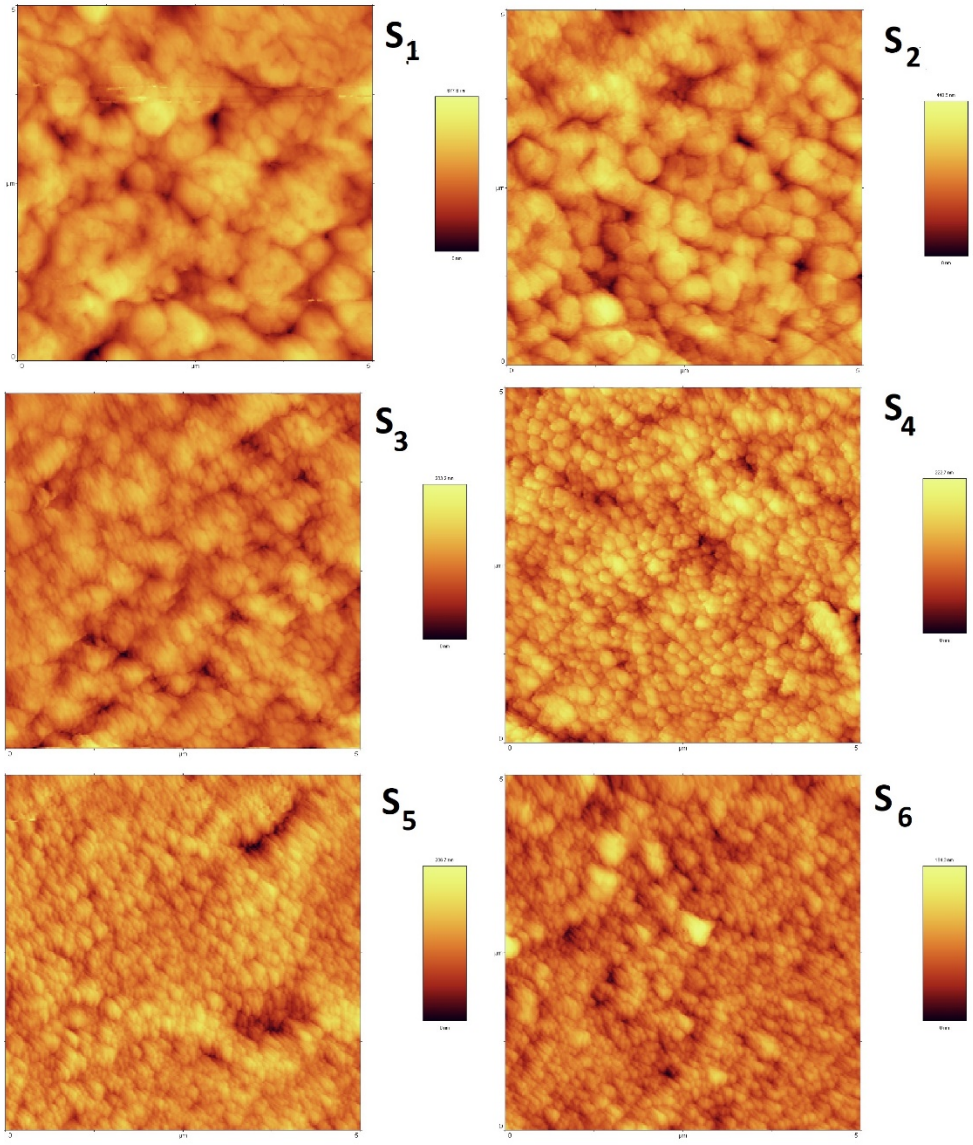

Figure 6-a

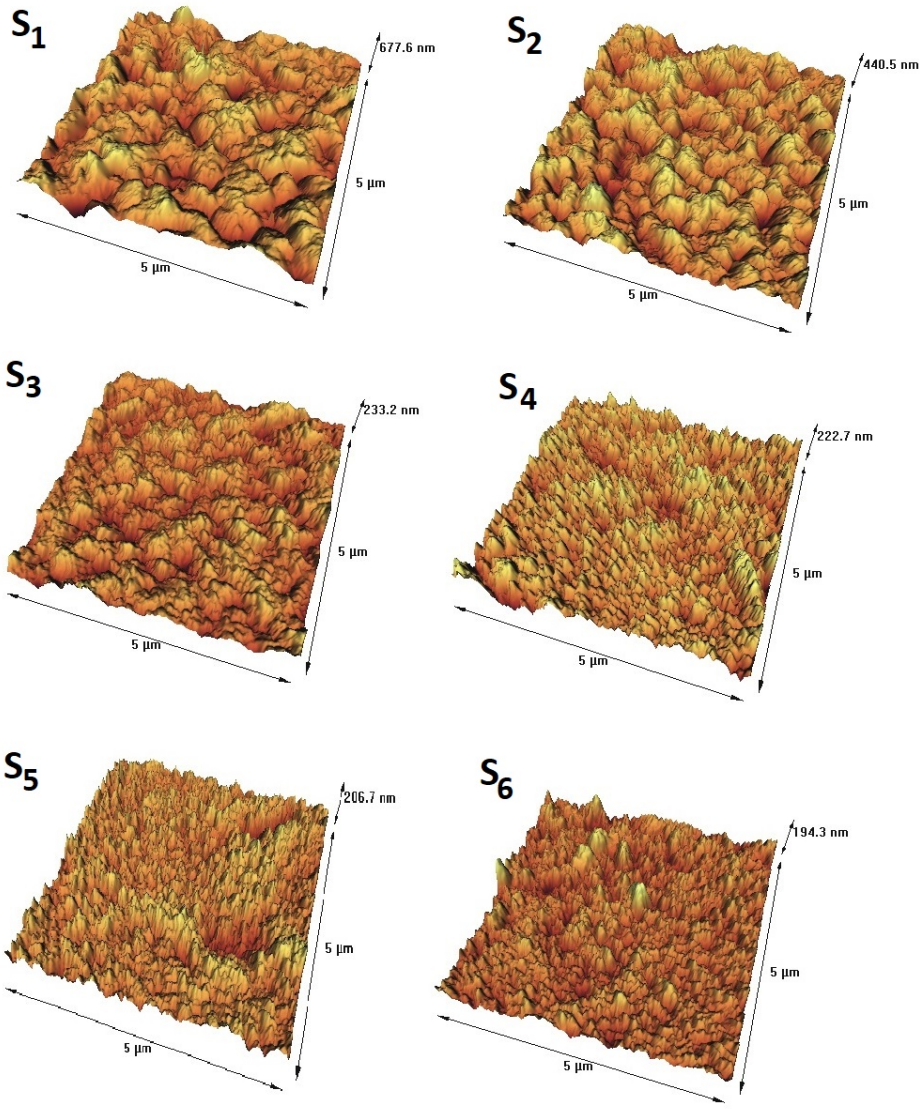
S1
677.6 nm
5 µm
5 µm
S2
440.5 nm
5 µm
5 µm
S3
233.2 nm
5 µm
5 µm
S4
222.7 nm
5 µm
5 µm
S5
206.7 nm
5 µm
5 µm
S6
194.3 nm
5 µm
5 µm

Figure 6-b

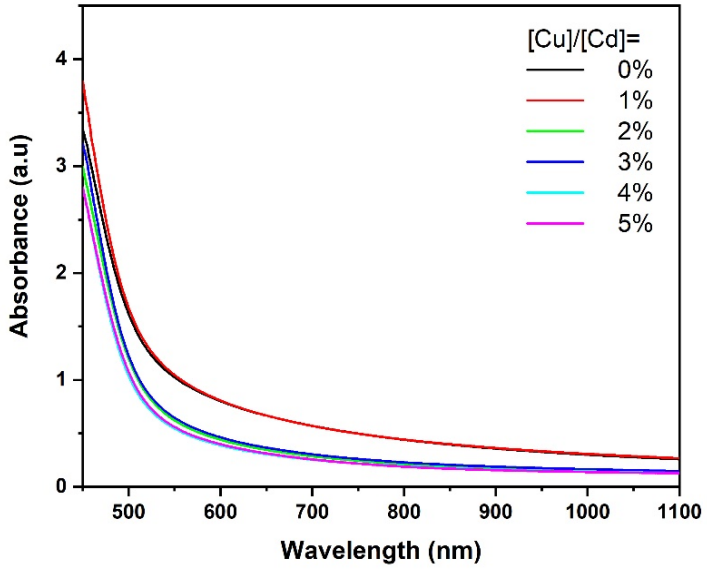
[Cu]/[Cd]=
0%
1%
2%
3%
4%
5%
Absorbance (a.u)
Wavelength (nm)
0
1
2
3
4
500
600
700
800
900
1000
1100

Figure 7

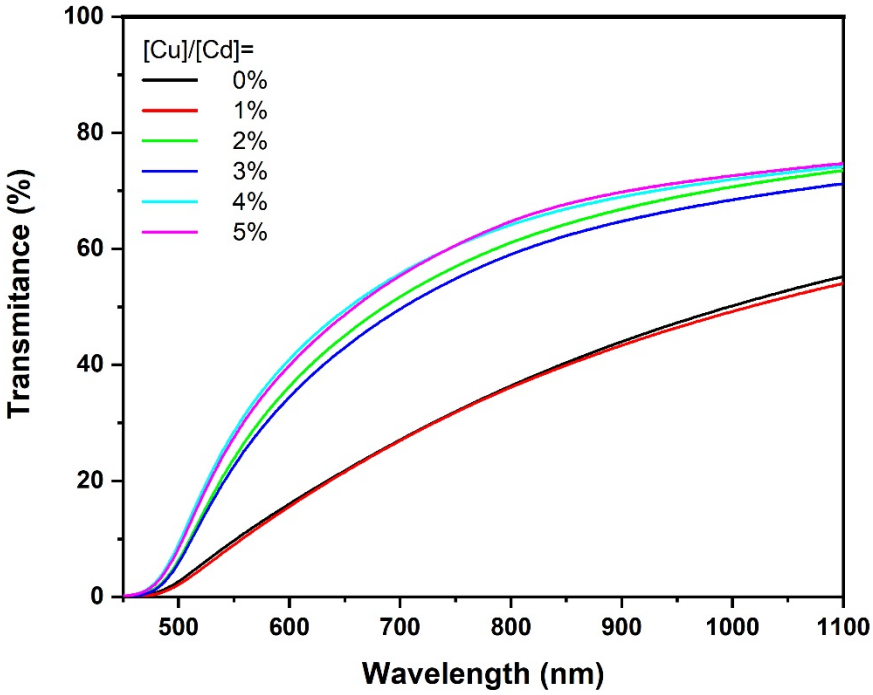
[Cu]/[Cd]=
0%
1%
2%
3%
4%
5%
Transmitance (%)
Wavelength (nm)
100
80
60
40
20
0
500
600
700
800
900
1000
1100

Figure 8

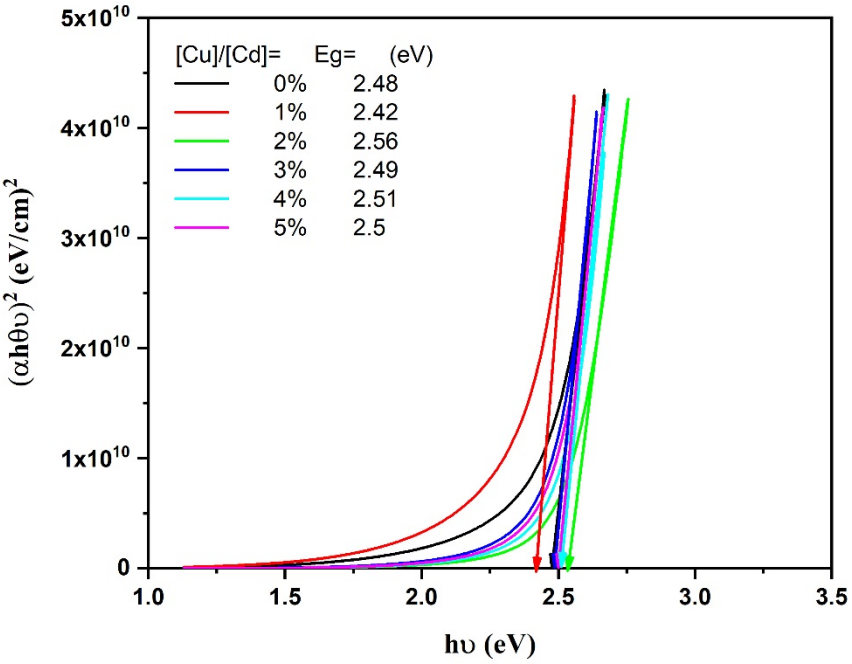
[Cu]/[Cd]= Eg= (eV)
0% 2.48
1% 2.42
2% 2.56
3% 2.49
4% 2.51
5% 2.5
5x10^10
4x10^10
3x10^10
2x10^10
1x10^10
0
1.0
1.5
2.0
2.5
3.0
3.5
(αhθυ)^2 (eV/cm)^2
hυ (eV)

Figure 9

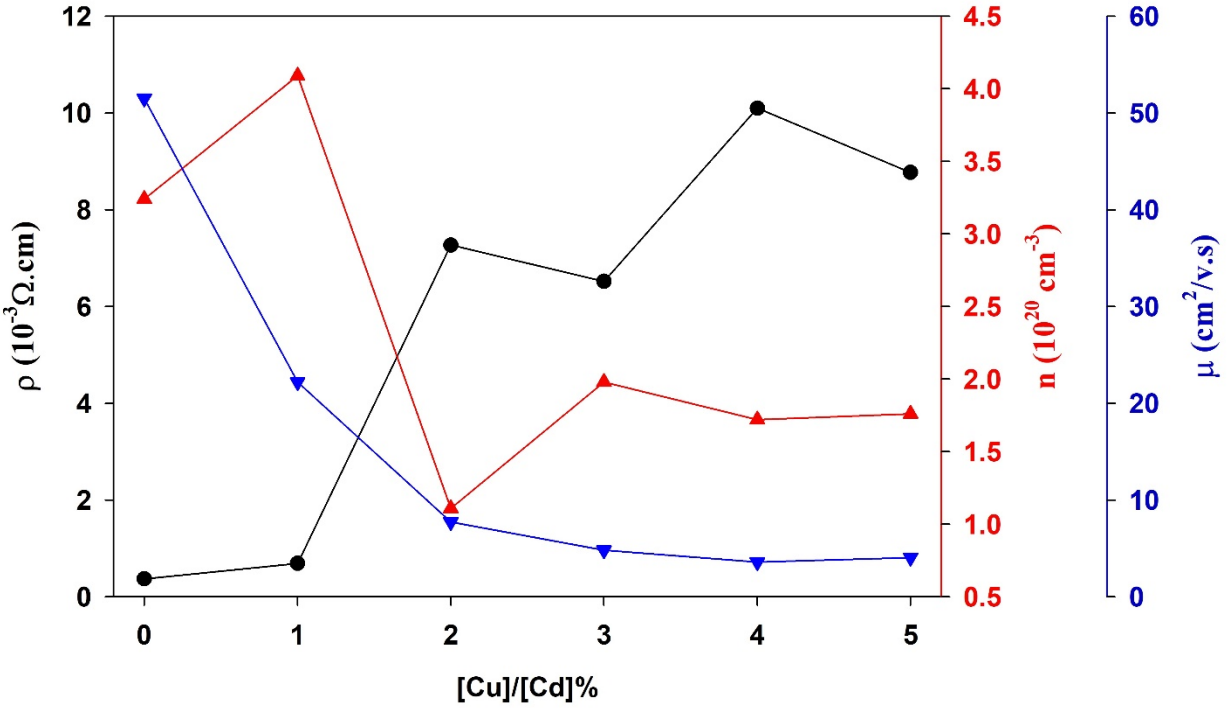
ρ (10^-3 Ω.cm)
n (10^20 cm^-3)
μ (cm^2/v.s)
[Cu]/[Cd]%
0
1
2
3
4
5
0
2
4
6
8
10
12
0.5
1.0
1.5
2.0
2.5
3.0
3.5
4.0
4.5
0
10
20
30
40
50
60

Figure 10

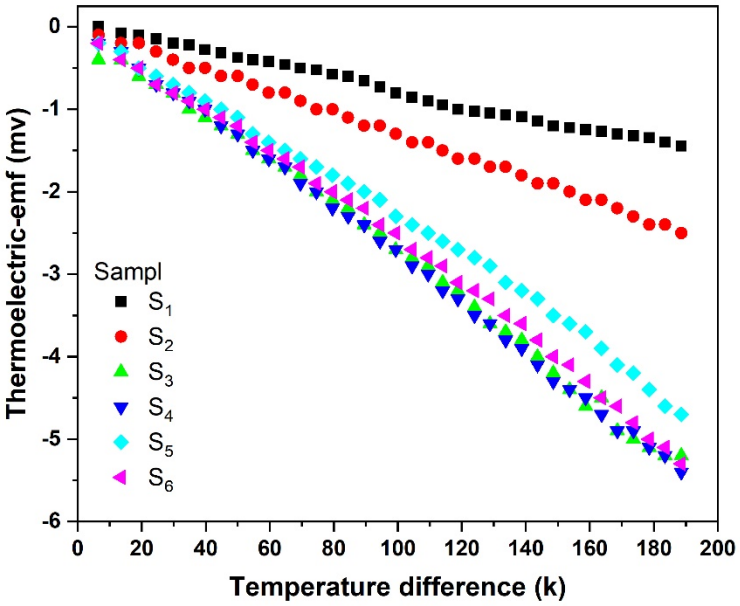
Thermoelectric-emf (mv)
Temperature difference (k)
Sampl
S1
S2
S3
S4
S5
S6
0
-1
-2
-3
-4
-5
-6
0
20
40
60
80
100
120
140
160
180
200

Figure 11

Table 1

Sample	(hkl)	2 θ(°)	FWHM(°)	Ds	D_{H-W} (nm)	ε ($\times 10^{-3}$)	δ ($\times 10^{15}$) Lines/m^2
S_1	(111)	33.031	0.561	14.76	19.26	15.08	2.7
	(200)	38.357	0.653	12.88			
	(220)	55.335	0.82	10.93			
	(311)	65.996	0.98	9.66			
	(222)	69.33	0.79	12.22			
S_2	(111)	33.019	0.569	14.56	19.46	16.87	2.64
	(200)	38.342	0.704	11.94			
	(220)	55.343	0.81	11.07			
	(311)	66.008	0.97	9.762			
	(222)	69.34	0.98	9.85			
S_3	(111)	33.057	0.555	14.93	19.33	13.74	2.68
	(200)	38.377	0.632	13.3			
	(220)	55.383	0.73	12.29			
	(311)	66.041	0.9	10.52			
	(222)	69.39	0.84	11.5			
S_4	(111)	33.034	0.484	17.11	19.41	7.93	2.65
	(200)	38.362	0.566	14.86			
	(220)	55.348	0.601	14.92			
	(311)	66.001	0.69	13.72			
	(222)	69.326	0.66	14.63			
S_5	(111)	33.036	0.506	16.37	18.83	7.68	2.82
	(200)	38.354	0.566	14.85			
	(220)	55.357	0.6	14.95			
	(311)	66.002	0.69	13.72			
	(222)	69.323	0.69	13.99			
S_6	(111)	33.129	0.529	15.66	17.45	4.43	3.28
	(200)	38.448	0.569	14.78			
	(220)	55.413	0.55	16.31			
	(311)	66.047	0.65	14.57			
	(222)	69.348	0.7	13.79			

Table 2

sample	t (nm)	Grain size (nm)	Roughness (nm)	RMS surface roughness (nm)
S1	750	472	162.74	195.37
S2	590	324	89.44	118.09
S3	902	98	55.05	66.33
S4	660	73	90.58	111.14
S5	660	51	70.18	88.41
S6	612	38	54.46	64.95

Table 3

sample	t (nm)	E_g (eV)	R_s $\left(\frac{\Omega}{\square}\right)$	ρ ($\times 10^{-3}$ Ω.cm)	n ($\times 10^{20}$ cm^{-3})	μ $\left(\frac{cm^2}{v.s}\right)$	Seebeck coefficient ($\times 10^{-5}$ v/k)
S1	750	2.48	4.98	0.37	3.24	51.5	-0.83
S2	590	2.42	11.7	0.69	4.09	22.2	-1.37
S3	902	2.56	80.6	7.27	1.11	7.73	-2.73
S4	660	2.49	99	6.52	1.98	4.83	-2.7
S5	660	2.51	1.54×10^2	10.1	1.72	3.6	-2.31
S6	612	2.5	1.44×10^2	8.77	1.76	4.05	-2.52

Figures

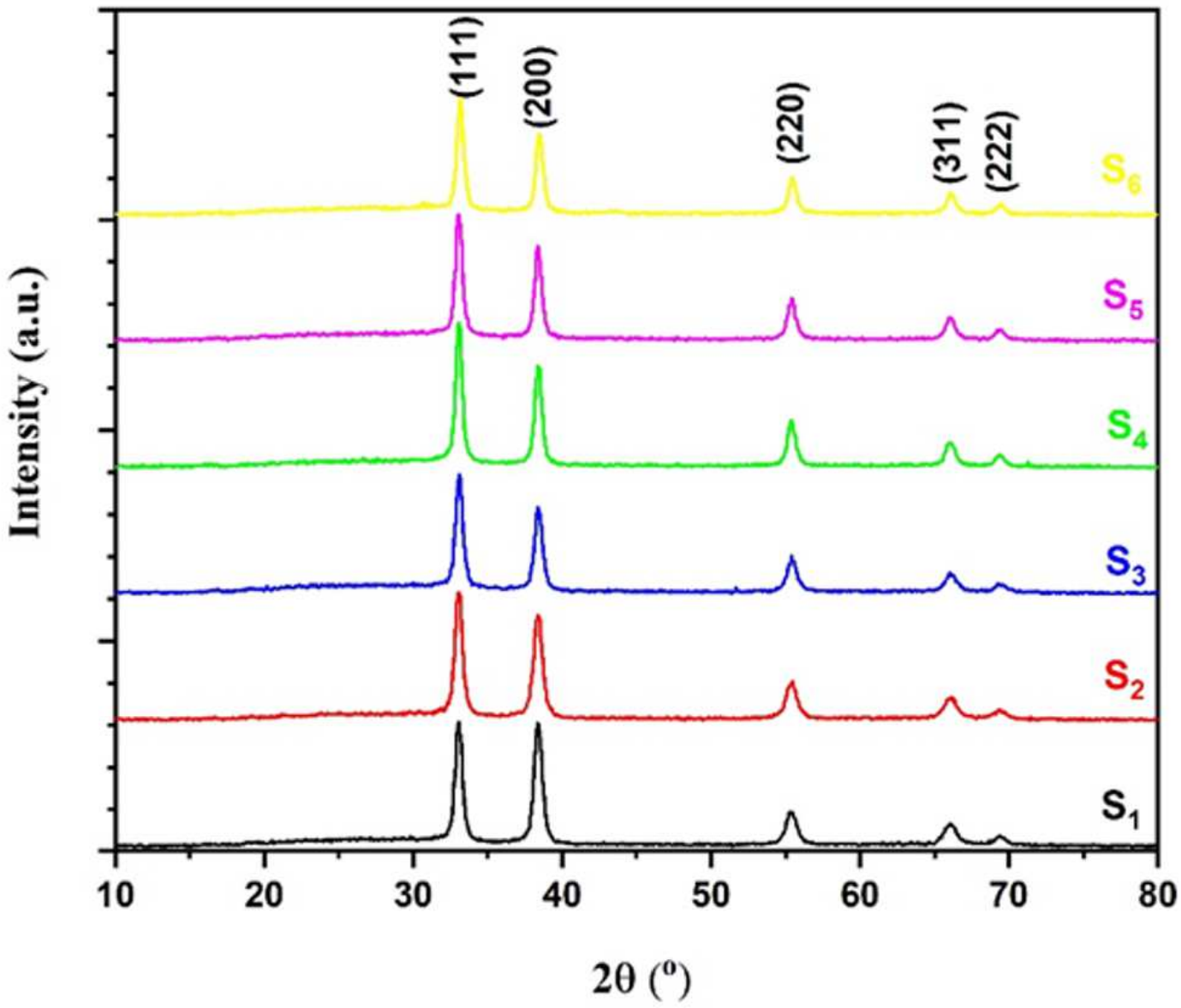

Figure 1

XRD patterns for samples S1, S2, S3, S4, S5, and S6

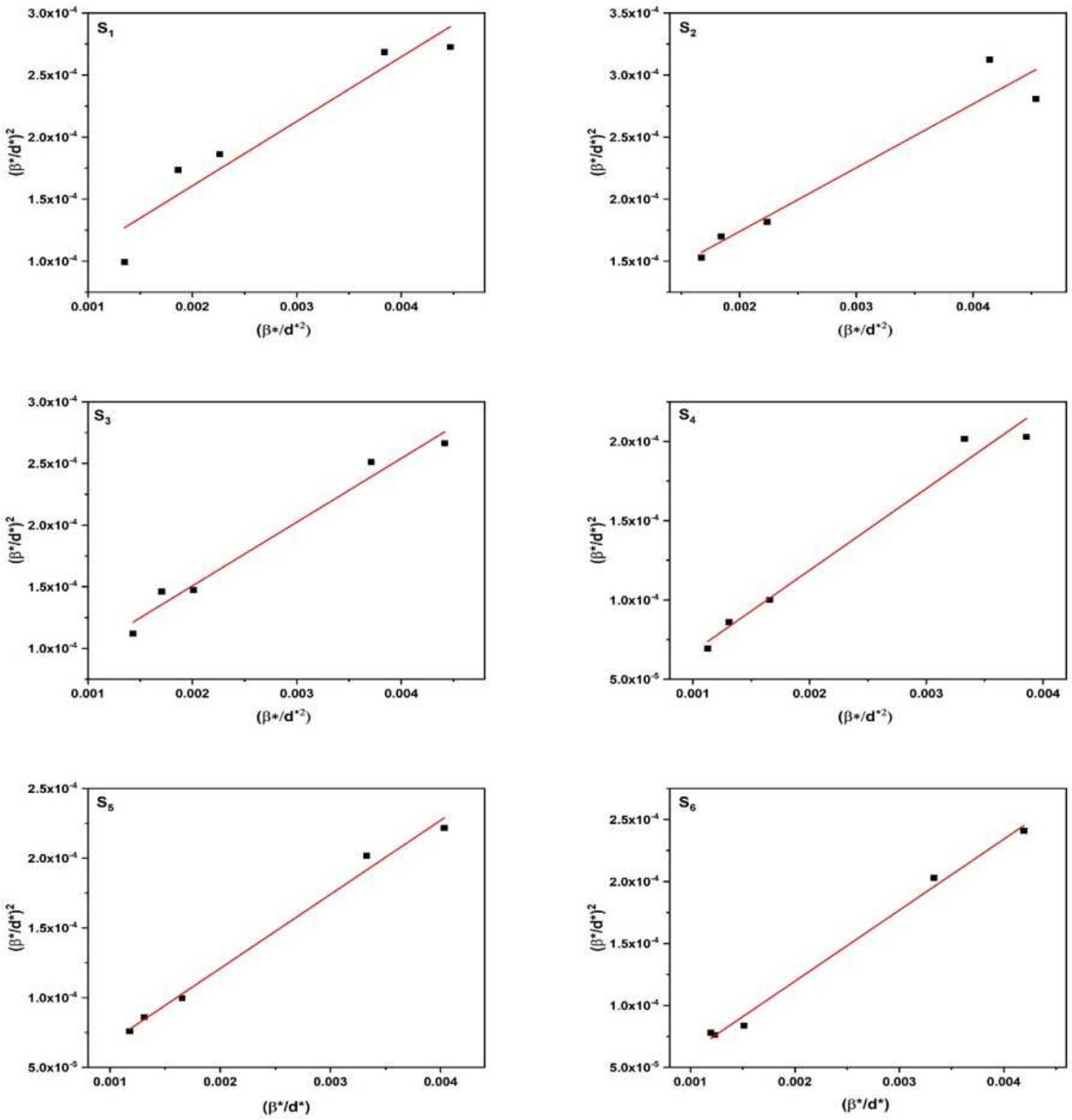

Figure 2

Typical Halder-Wagner plots of samples S1, S2, S3, S4, S5, and S6

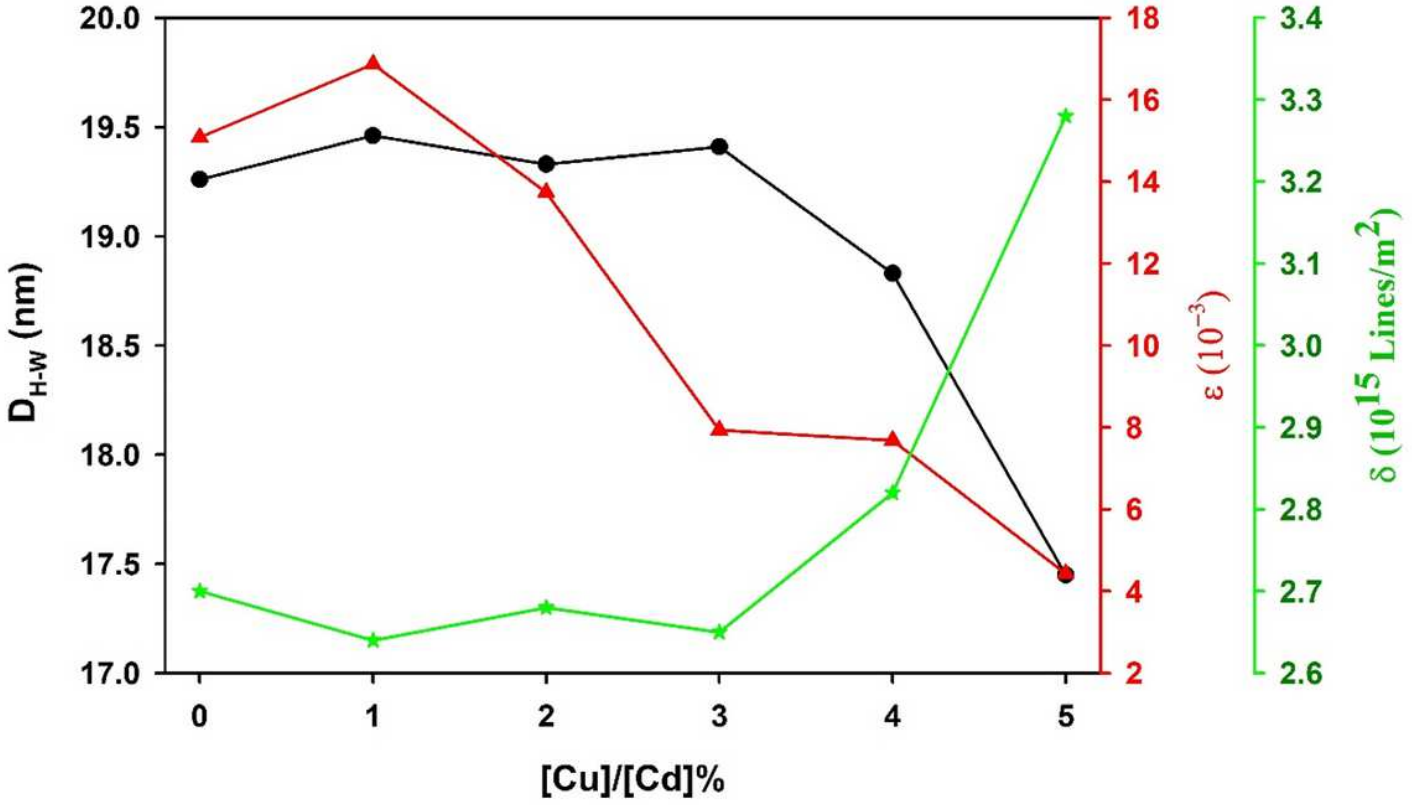

Figure 3

Variations of the average crystallite size (DH-W), dislocation density (δ), and strain (ε) as a function of the [Cu]/[Cd] % molar ratio in the thin films

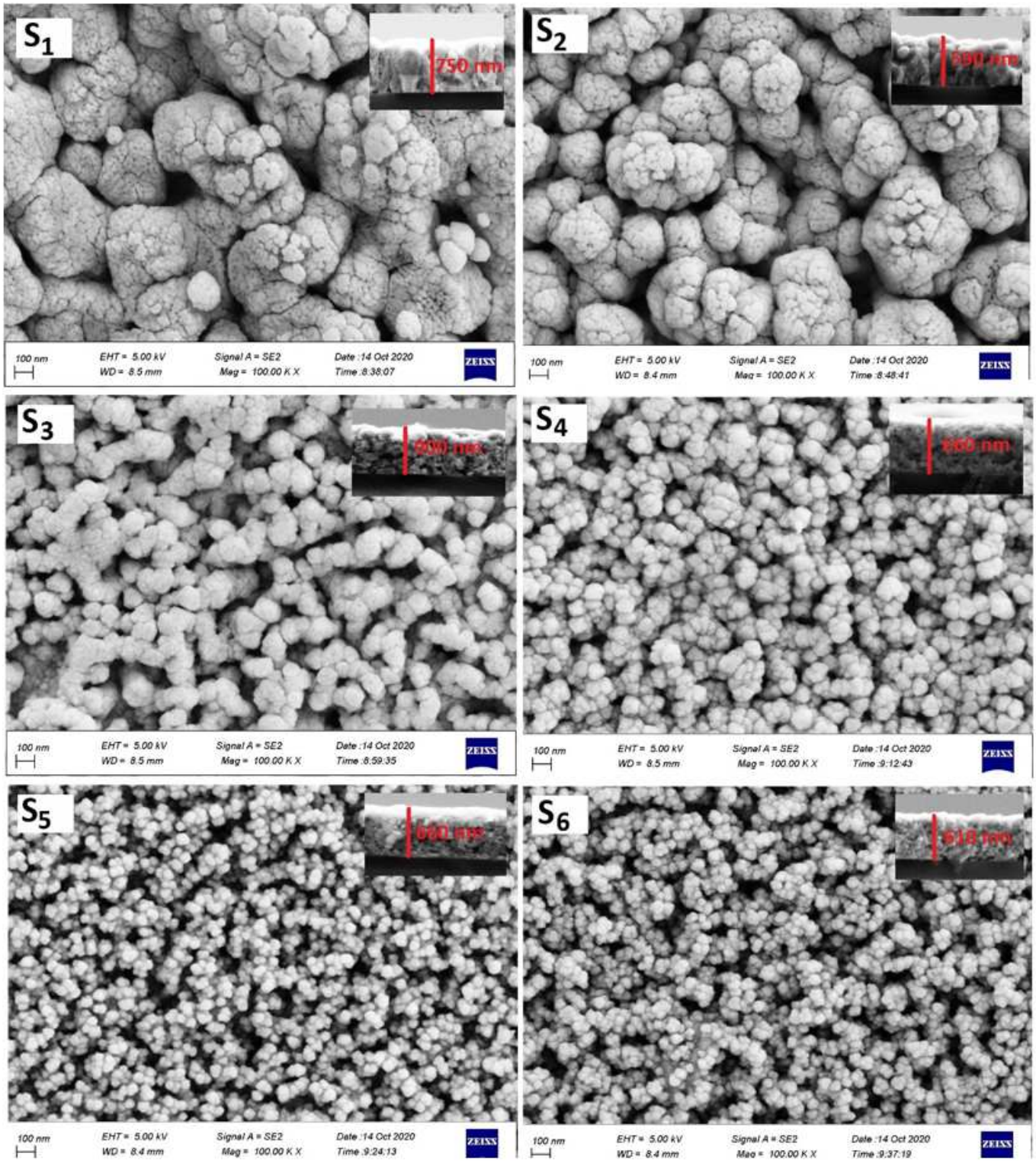

Figure 4

Top view FE-SEM and cross-section FE-SEM images of samples S1, S2, S3, S4, S5, and S6

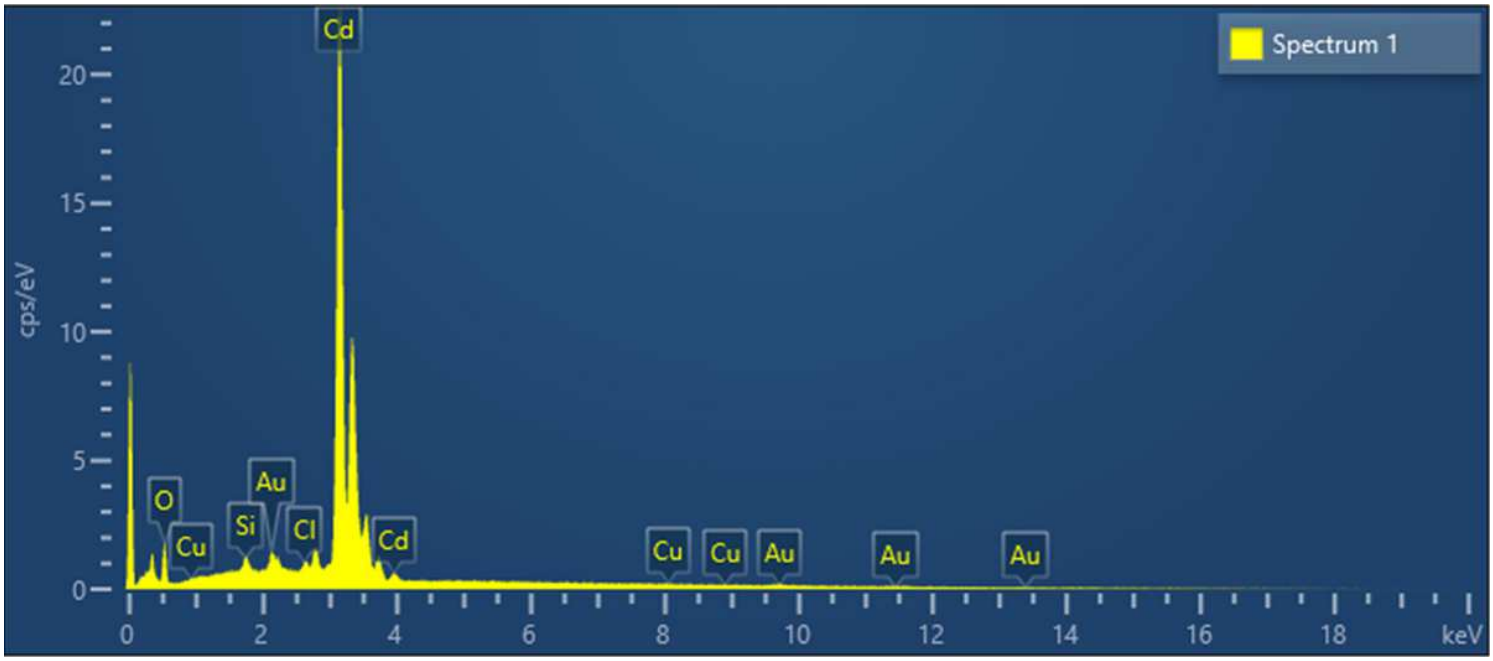

Figure 5

Energy-dispersive X-ray analysis spectra of a thin film with [Cu]/[Cd]=1%

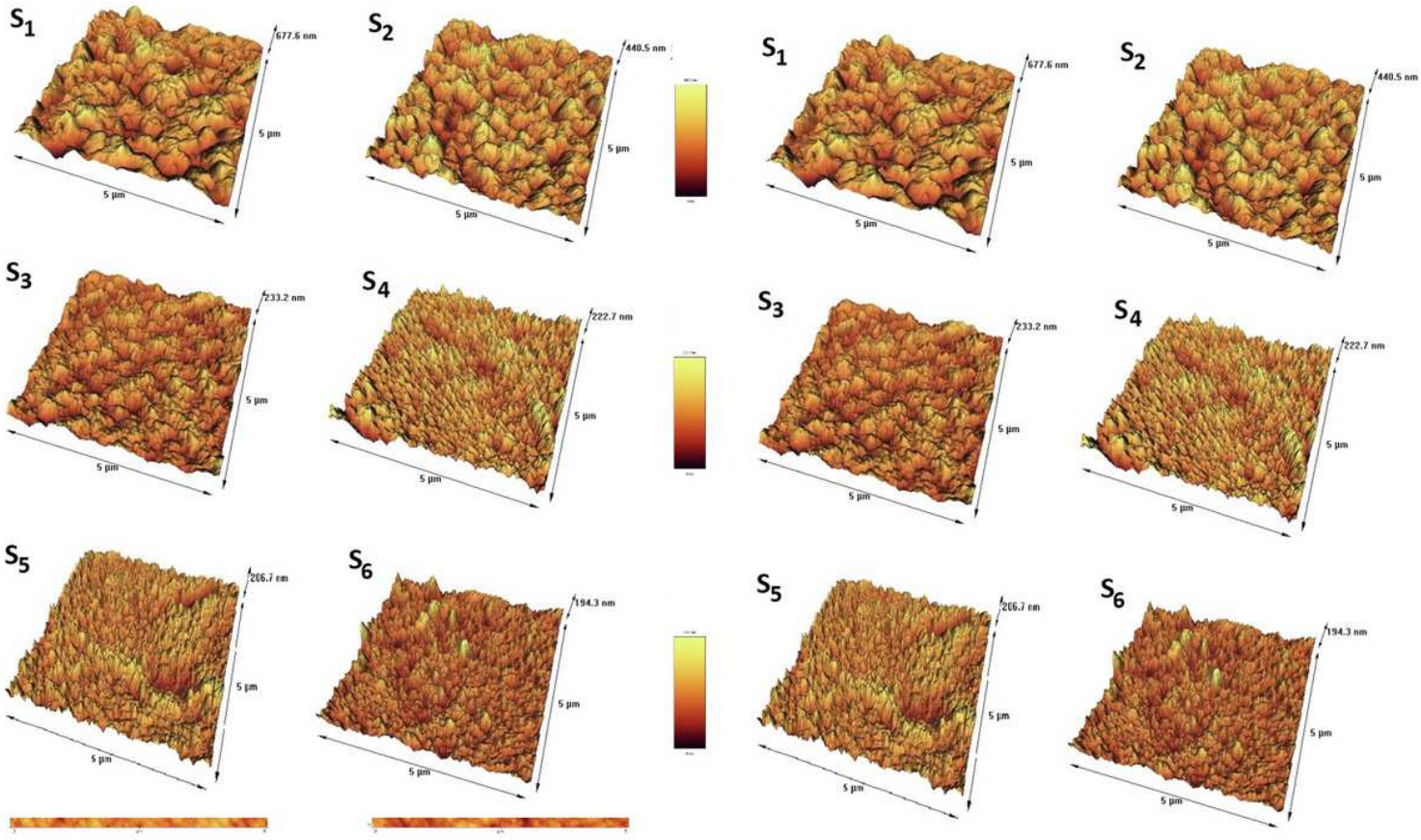

Figure 6

AFM images of samples S1, S2, S3, S4, S5, and S6 (a) two dimensional and (b) three dimensional

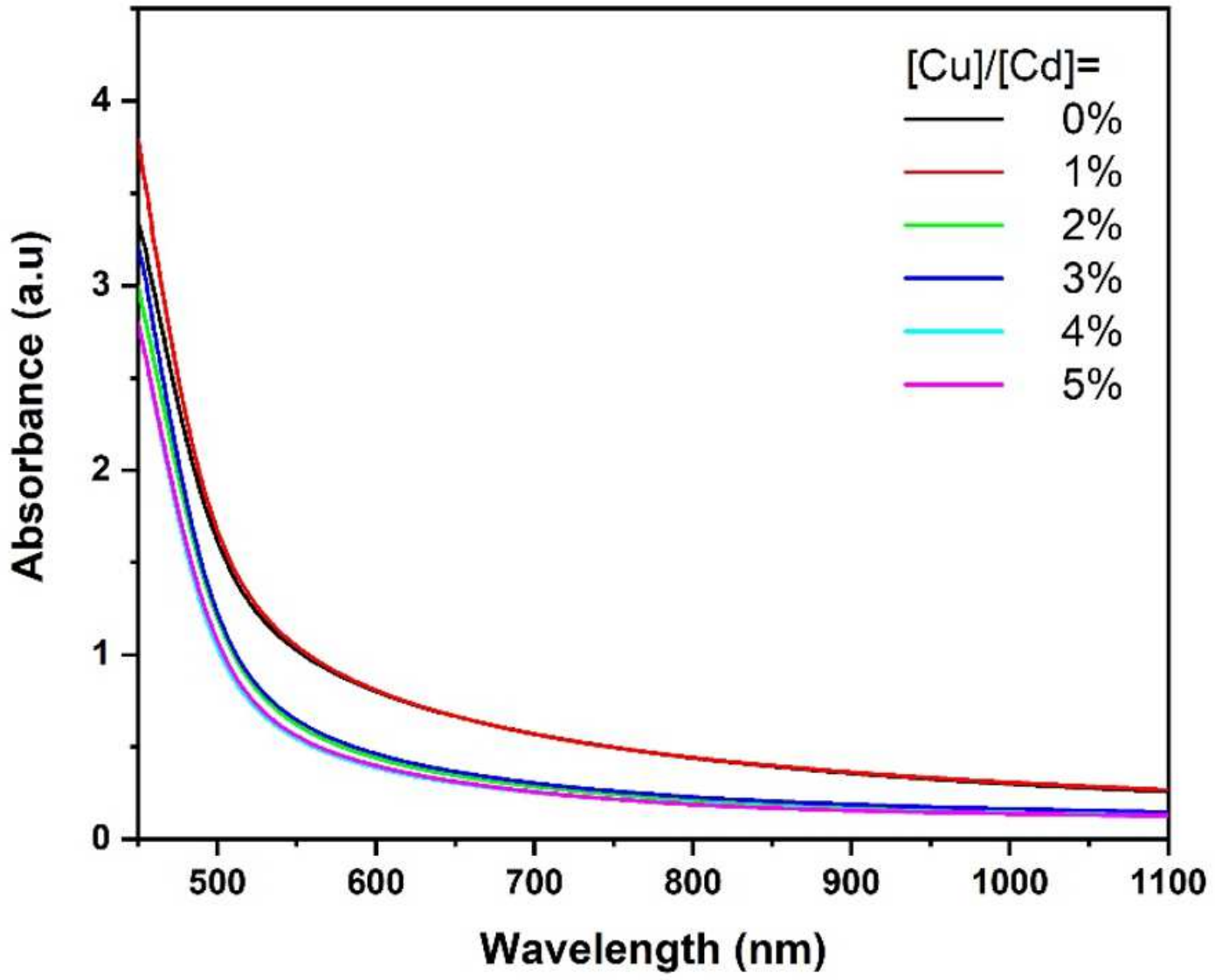

Figure 7

Variation of absorption versus wavelength in samples S1, S2, S3, S4, S5, and S6

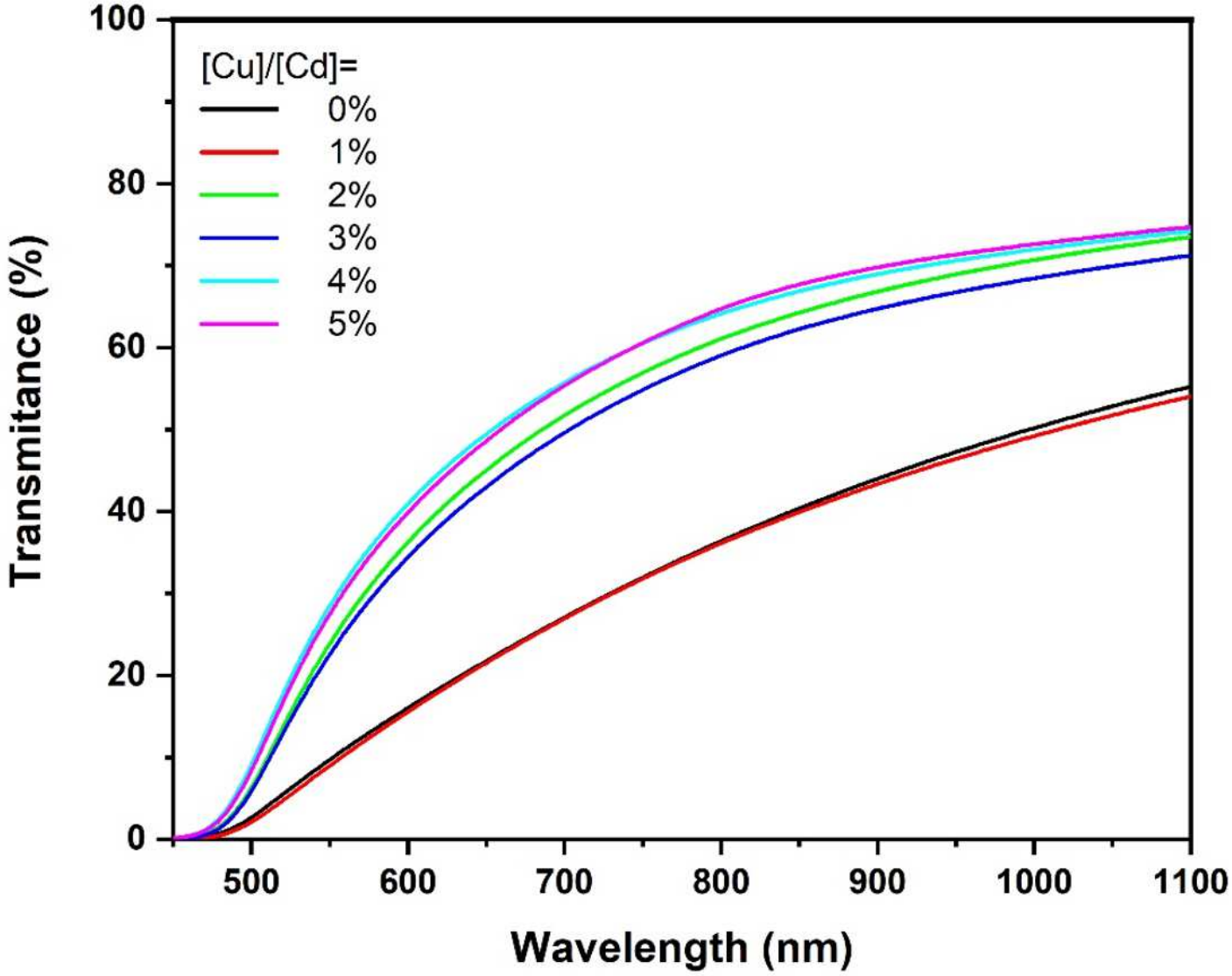

Figure 8

Variation of transmittance versus wavelength in samples S1, S2, S3, S4, S5, and S6

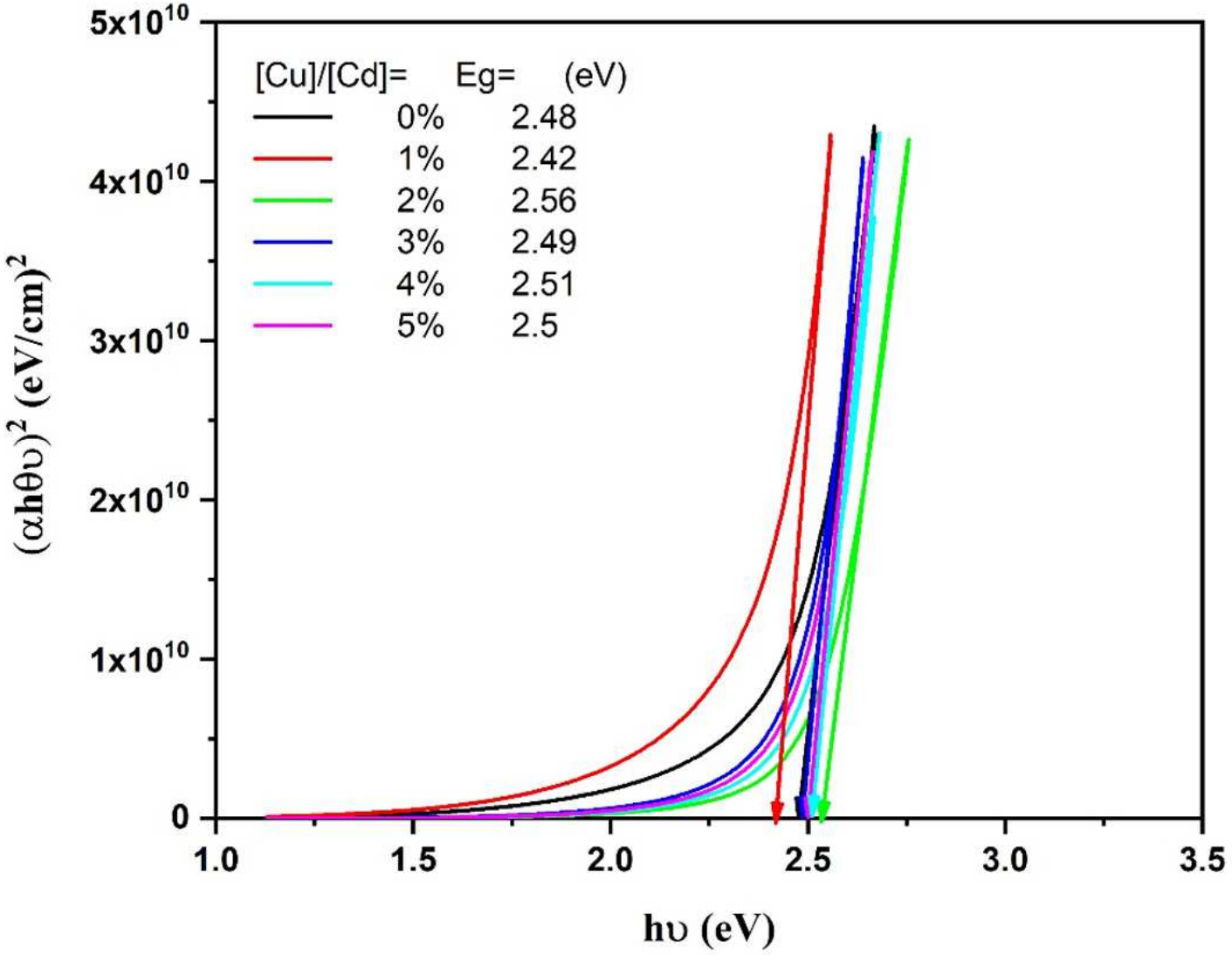

Figure 9

Plots of (αhϑ)^2 versus hϑ for samples S1, S2, S3, S4, S5, and S6

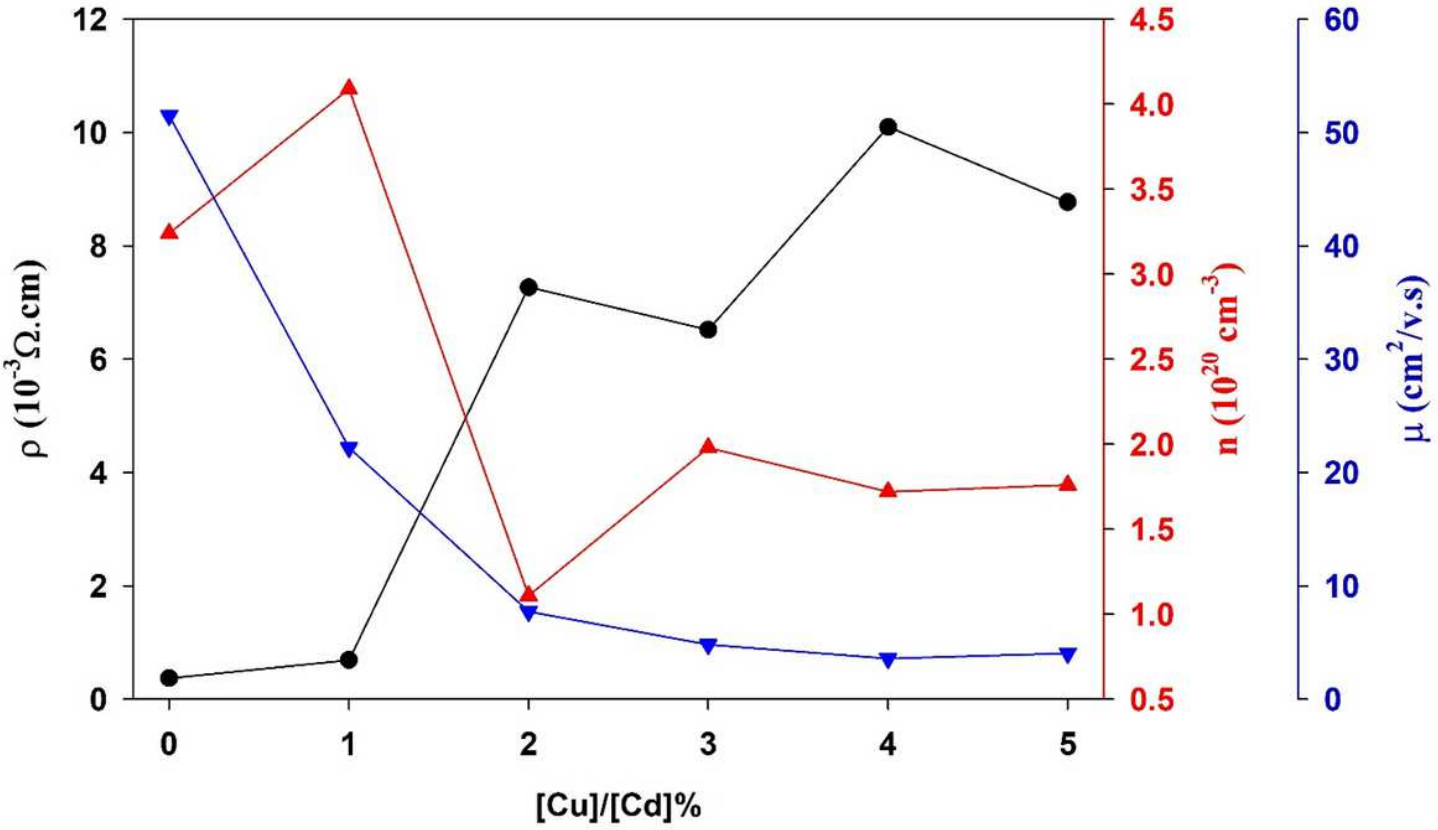

Figure 10

Variations of resistivity (ρ), carrier concentration (n), and electron mobility (l) as a function of the [Cu]/[Cd] % molar ratio in the thin films

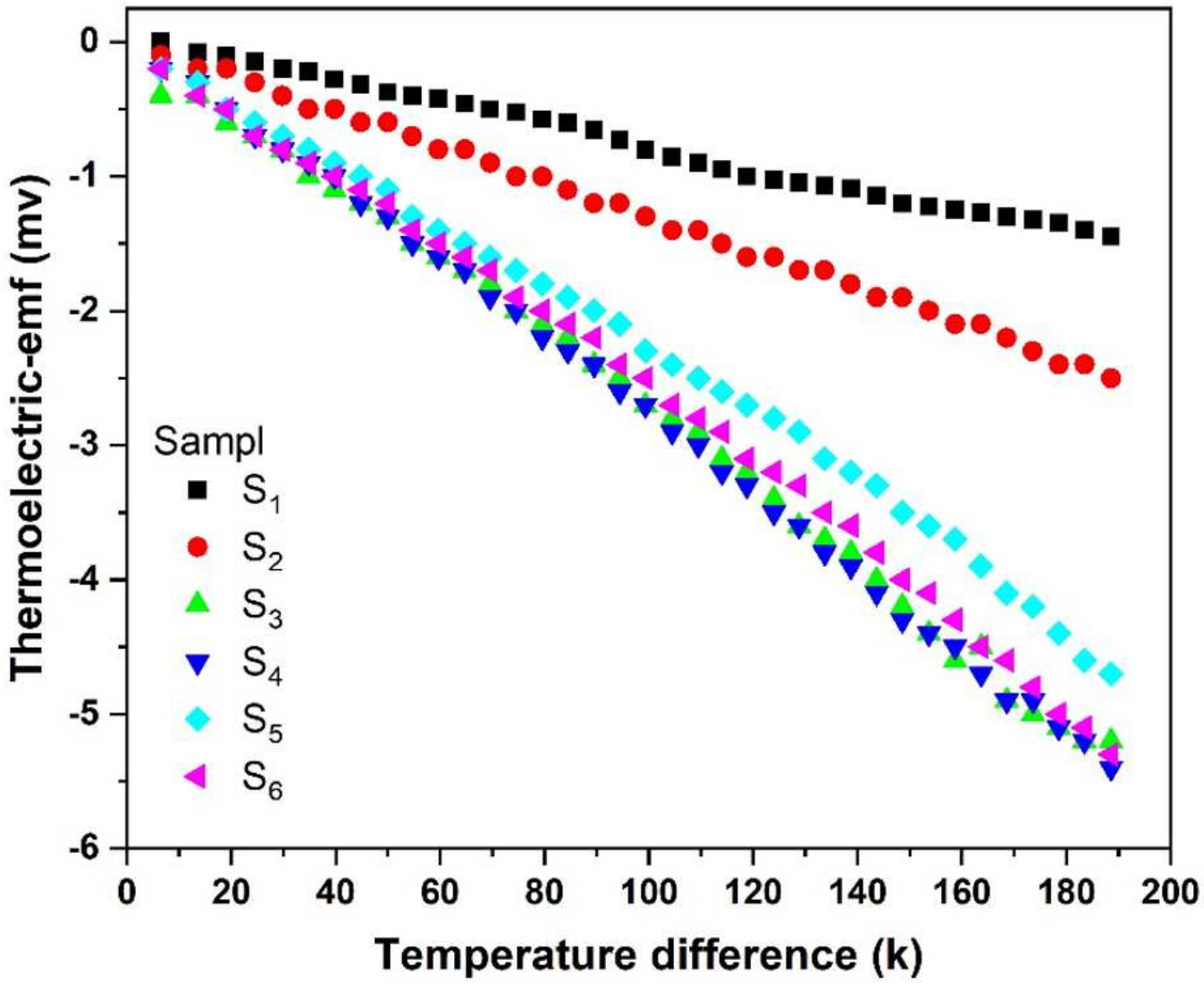

Figure 11

Variation of the thermoelectric emf versus the temperature difference in samples S1, S2, S3, S4, S5, and S6